



## 1 **Biogeochemical Impact of Cable Bacteria on Coastal Black Sea Sediment**

2 **Martijn Hermans<sup>1</sup>, Nils Risgaard-Petersen<sup>2,3</sup>, Filip J.R. Meysman<sup>4,5</sup> and Caroline P. Slomp<sup>1</sup>**

3 <sup>1</sup>Department of Earth Sciences, Faculty of Geosciences, Utrecht University, P.O Box 80021, 3508 TA  
4 Utrecht, the Netherlands

5 <sup>2</sup>Center for Geomicrobiology, Section for Microbiology, Department of Bioscience, Aarhus  
6 University, Aarhus, Denmark

7 <sup>3</sup>Center for Electromicrobiology, Section for Microbiology, Department of Bioscience, Aarhus  
8 University, Aarhus, Denmark

9 <sup>4</sup>Center of Excellence for Microbial Systems Technology, Department of Biology, University of  
10 Antwerp, Wilrijk, Belgium

11 <sup>5</sup>Department of Biotechnology, Delft University of Technology, Delft, the Netherlands

### 12 **ABSTRACT**

13 Cable bacteria can strongly alter sediment biogeochemistry. Here, we used laboratory  
14 incubations to assess whether cable bacteria can establish in iron (Fe) monosulphide-poor coastal  
15 Black Sea sediment and to determine the impact of their activity on the cycling of Fe, phosphorus (P)  
16 and sulphur (S). Microsensor depth profiles of oxygen, sulphide and pH in combination with electric  
17 potential profiling and FISH analyses showed a rapid development (<5 days) of cable bacteria,  
18 followed by a long period of activity (>200 days). During most of the experiment, the current density  
19 correlated linearly with the oxygen demand. Sediment oxygen uptake was attributed to activity of  
20 cable bacteria and the oxidation of reduced products from anaerobic degradation of organic matter,  
21 such as ammonium. Pore water sulphide was low (<5  $\mu\text{M}$ ) throughout the experiment. Sulphate  
22 reduction acted as the main source of sulphide for cable bacteria. Pore water  $\text{Fe}^{2+}$  reached levels of up  
23 to 1.7 mM during the incubations, due to the dissolution of FeS (30%) and siderite, an Fe carbonate  
24 mineral (70%). Following upward diffusion of  $\text{Fe}^{2+}$ , a surface enrichment of Fe oxides formed. Hence,  
25 besides FeS, siderite may act as a major source of Fe for Fe oxides in coastal surface sediments where  
26 cable bacteria are active. Using  $\mu\text{XRF}$ , we show that the enrichments in Fe oxides induced by cable



27 bacteria are located in a thin subsurface layer of 0.3 mm. We show that similar subsurface layers  
28 enriched in Fe and P are also observed at field sites where cable bacteria were recently active and  
29 little bioturbation occurs. This suggests that such subsurface Fe oxide layers, which are not always  
30 visible to the eye, could potentially be a marker for recent activity of cable bacteria.

31 Key words: cable bacteria, elemental cycling, solute fluxes, iron

## 32 1. INTRODUCTION

33 Depletion of oxygen ( $O_2$ ) in bottom waters of coastal areas is increasing worldwide, as a  
34 consequence of eutrophication and climate change (Diaz and Rosenberg 2008; Schmidtko et al. 2017;  
35 Breitburg et al. 2018). Low  $O_2$  can lead to the development of coastal ‘dead zones’ characterised by  
36 recurrent mortality of marine life (Rabalais et al. 2002; Diaz and Rosenberg 2008). Progressive  
37 eutrophication induces a characteristic response of coastal systems with transient and seasonal  
38 hypoxia ( $O_2 < 63 \mu\text{M}$ ) transitioning into permanent anoxia ( $O_2 = 0 \mu\text{M}$ ). In this later stage, free  
39 sulphide ( $H_2S$ ) may escape from the sediment and accumulate in the bottom water, a condition  
40 referred to as euxinia (Diaz and Rosenberg 2008; Kemp et al. 2009; Rabalais et al. 2014). As  $H_2S$  is  
41 highly toxic to higher fauna, the development of euxinia may aggravate the ecological consequences.  
42 However, the presence of iron (Fe) and manganese (Mn) oxides in surface sediments may delay this  
43 transition towards euxinia by removing  $H_2S$  and thus preventing an efflux of  $H_2S$  to the overlying  
44 water (Kristiansen et al. 2002; Kristensen et al. 2003; Diaz and Rosenberg 2008).

45 Cable bacteria are multicellular filamentous sulphur(S)-oxidising bacteria (Pfeffer et al. 2012)  
46 that strongly enhance the formation of Fe and Mn oxides and efficiently remove  $H_2S$  from surface  
47 sediments (Risgaard-Petersen et al. 2012; Seitaj et al. 2015; Sulu-Gambari et al. 2016a). Cable  
48 bacteria belong to the *Desulfobulbaceae* family of the Deltaproteobacteria (Trojan et al. 2016;  
49 Kjeldsen et al. 2019). Cable bacteria can spatially link the oxidation of  $H_2S$  in deeper sediments to the  
50 reduction of  $O_2$  near the sediment-water interface by transporting electrons over centimetre scale  
51 distances (Pfeffer et al. 2012) through a conductive fibre network that is embedded in the cell  
52 envelope (Meysman et al. 2019). This spatial coupling of surficial  $O_2$  reduction with  $H_2S$  oxidation at



53 several centimetres depth provides cable bacteria a competitive advantage over other S-oxidising  
54 bacteria in aquatic environments (Meysman 2018). Cable bacteria have been documented in a range  
55 of fresh water (Risgaard-Petersen et al. 2015; Müller et al. 2016) and marine environments (Malkin et  
56 al. 2014; Burdorf et al. 2017), however, they appear to be particularly active in sediments overlain by  
57 seasonally hypoxic bottom waters (Seitaj et al. 2015; Burdorf et al. 2018).

58 The metabolic activity of cable bacteria establishes an electrical circuit in the sediment, which  
59 involves an electron current through the cable bacteria filaments (Bjerg et al. 2018), and an ionic  
60 current through the pore water in the opposite direction (Naudet and Revil 2005; Revil et al. 2010;  
61 Risgaard-Petersen et al. 2012). As a consequence, an electric potential (EP) is generated in the  
62 sediment, which can be used as a reliable indicator for activity of cable bacteria (Risgaard-Petersen et  
63 al. 2014).

64 Cable bacteria activity additionally generates a distinct biogeochemical signature, that can be  
65 assessed by pH, O<sub>2</sub> and H<sub>2</sub>S depth profiling (Nielsen et al. 2010). Their activity leads to the  
66 development of a suboxic zone (i.e. a zone where O<sub>2</sub> and H<sub>2</sub>S are both absent), and also induces a pH  
67 profile that strongly changes with depth. Cathodic O<sub>2</sub> reduction ( $O_2 + 4H^+ + 4e^- \rightarrow 2H_2O$ ) in the oxic  
68 zone of the sediment results in a pH maximum (~9) due to proton consumption, whereas anodic  
69 sulphide oxidation ( $H_2S + 4 H_2O \rightarrow SO_4^{2-} + 10H^+ + 8e^-$ ) causes a pH minimum (<6.5) in the anoxic  
70 zone (Fig. 1A; Nielsen et al. 2010; Meysman et al. 2015).

71 The presence of cable bacteria in sediments can strongly impact the elemental cycling of Fe,  
72 Mn, Ca and S (Risgaard-Petersen et al. 2012; Seitaj et al. 2015; Rao et al. 2016; Sulu-Gambari et al.  
73 2016a; van de Velde et al. 2016). Pore water acidification induced by cable bacteria activity can lead  
74 to dissolution of calcium (Ca) carbonates, Fe carbonates (siderite), Mn carbonates and FeS in the zone  
75 where the pH is low, thus generating high concentrations of Fe<sup>2+</sup> and Mn<sup>2+</sup> in the pore water  
76 (Risgaard-Petersen et al. 2012; Rao et al. 2016). When these dissolved species diffuse upward this can  
77 lead to strong enrichments of Fe and Mn oxides upon contact with O<sub>2</sub> or for dissolved Fe<sup>2+</sup>, also upon  
78 contact with Mn oxides (Wang and Van Cappellen 1996; Seitaj et al. 2015; Sulu-Gambari et al.



79 2016a). These metal oxides are capable of efficiently buffering the benthic release of H<sub>2</sub>S and  
80 phosphate (HPO<sub>4</sub><sup>2-</sup>) during periods with low bottom water O<sub>2</sub>. This so-called ‘firewall’ for H<sub>2</sub>S and  
81 alteration of the timing of HPO<sub>4</sub><sup>2-</sup> release linked to this buffering can play a key role in regulating  
82 water quality in seasonally hypoxic coastal systems (Seitaj et al. 2015; Sulu-Gambari et al. 2016b;  
83 Hermans et al. 2019a).

84 In coastal sediments, O<sub>2</sub> typically penetrates to a depth of only several mm’s below the  
85 sediment-water interface (Rasmussen and Jørgensen 1992; Rabouille et al. 2003; Glud 2008). This  
86 also holds true for sediments inhabited by active cable bacteria (Nielsen et al. 2010; Pfeffer et al.  
87 2012; Larsen et al. 2015). Hence, the oxidation of upward diffusing Fe<sup>2+</sup> and Mn<sup>2+</sup> is expected to take  
88 place below and not at the sediment-water interface. We hypothesise that, as a consequence, in the  
89 initial stages of cable bacteria activity and in the absence of bioturbation, most Fe and Mn oxide  
90 enrichments will be restricted to a thin subsurface layer of the sediment. However, the sample  
91 resolution and timing of the collection of solid phase data in field and laboratory studies published so  
92 far do not allow an assessment of this hypothesis.

93 Cable bacteria are suggested to thrive in coastal sediments characterised by high rates of H<sub>2</sub>S  
94 production due to high rates of organic matter mineralisation (Malkin et al. 2014; Burdorf et al. 2017;  
95 Hermans et al. 2019a). Laboratory and model studies have shown that the dissolution of FeS accounts  
96 for 12 to 94% of the H<sub>2</sub>S consumed by cable bacteria, while the other source is H<sub>2</sub>S production from  
97 the reduction of SO<sub>4</sub><sup>2-</sup> (Risgaard-Petersen et al. 2012; Meysman et al. 2015; Burdorf et al. 2018). At  
98 present, it is not known if cable bacteria activity can establish in sediments that are relatively low in  
99 FeS and dissolved H<sub>2</sub>S.

100 In this study, we assess whether cable bacteria activity can establish in sediments that are  
101 relatively poor in FeS in an incubation experiment using siderite-bearing sediments from a coastal site  
102 in the Black Sea. The metabolic activity of cable bacteria is monitored using microsensor profiles of  
103 pH, O<sub>2</sub>, H<sub>2</sub>S and EP. We also use sediment Fe and P speciation and  $\mu$ XRF of resin-embedded  
104 sediments to test whether we find evidence for subsurface enrichments in Fe oxides and associated P.



105 We find a rapid establishment of cable bacteria (<5 days) and the development of an Fe oxide-rich  
106 subsurface layer, with the majority of the Fe ~70% supplied through dissolution of siderite induced by  
107 cable bacteria activity. The depth of the Fe oxide layer was directly related to the O<sub>2</sub> penetration depth  
108 and we propose that such subsurface enrichments in Fe, which also can contain P and Mn, can be used  
109 as a marker for recent cable bacteria activity.

## 110 **2. METHODS AND MATERIALS**

### 111 **2.1. Study Area and Experimental Set-up**

112 In September 2015, 16 sediment cores (ø10 cm) were retrieved at a coastal site on the north-  
113 western shelf of the Black Sea (27 m water depth; Fig. 1B; Table 1) using a multicorer (Oktopus  
114 GmbH, Germany) as described in Lenstra et al. (2019). The overlying water was discarded, and the  
115 upper 10 cm of the sediment was transferred into nitrogen purged aluminium bags that were sealed  
116 and stored at 4 °C for several months. The anoxic storage is expected to have led to the death of all  
117 macrofauna and most meiofauna (Coull and Chandler 2001; Riedel et al. 2012). Prior to incubation,  
118 the sediment was passed through a 4 mm sieve to remove large debris and homogenised.  
119 Subsequently, the sediment was transferred to 18 transparent polycarbonate cores (ø6 cm; 20 cm  
120 length).

121 The bottom 15 cm of these cores was filled with sediment and the upper 5 cm with overlying  
122 water. The cores were placed in two aquaria filled with artificial seawater (Instant Ocean Sea Salt +  
123 Ultra High Quality (UHQ) water) with a salinity of 17.9, identical to the bottom water salinity at the  
124 study site. The artificial sea water contained negligible concentrations of NH<sub>4</sub><sup>+</sup>, NO<sub>3</sub><sup>-</sup>, Fe, Mn and P as  
125 described in Atkinson (1997) and Hovanec and Coshland (2004). The aquaria were kept in the dark at  
126 a constant temperature (~20 °C), and the water was continuously aerated by two aquarium pumps.  
127 Sixteen out of eighteen cores were exposed to oxygenated overlying water in the aquaria, whereas the  
128 two remaining cores served as an anoxic control treatment. The control cores were tightly sealed with  
129 rubber stoppers, to prevent the growth of cable bacteria by excluding O<sub>2</sub> (Nielsen et al. 2010).



130            Sampling for pore water and solid-phase analyses was performed at eight time points over a  
131 total incubation period of 621 days. Each time point involved a three day procedure. On the first day,  
132 microsensor depth profiles of EP, O<sub>2</sub>, pH and H<sub>2</sub>S were obtained in two randomly selected oxic cores  
133 and the two anoxic control cores (O<sub>2</sub> profiling was not performed in the anoxic cores). On the second  
134 day, solute fluxes were measured in the same oxic cores that were used for microsensor depth  
135 profiling on the previous day. On the third day, the two cores were sectioned, of which only one core  
136 was processed further for pore water and solid-phase analyses. Photographs were taken at four time  
137 points (day 12; 33; 170 and 621) from one oxic core to follow the visual development of the surface  
138 sediment during the experiment.

### 139 **2.2. High-resolution Microsensor Depth Profiling**

140            High-resolution depth profiles of pH, O<sub>2</sub> and H<sub>2</sub>S were obtained (50- $\mu$ m depth resolution; 3  
141 replicate profiles per oxic core; 2 replicate profiles per anoxic core) using commercial micro  
142 electrodes (Unisense A.S., Denmark). The O<sub>2</sub> sensor was re-calibrated prior to each measurement,  
143 using saturated bottom water (100% [O<sub>2</sub>]) and the deeper sediment horizons (0% [O<sub>2</sub>]) as calibration  
144 points. Calibrations of the pH and H<sub>2</sub>S electrodes were performed as described in Hermans et al.  
145 (2019b). pH values are reported on the total scale. For depth profiling of EP (500- $\mu$ m resolution; 3  
146 replicates per core), micro electrodes were used that were custom built at Aarhus University, as  
147 described in Damgaard et al. (2014). A robust reference electrode (Ref-RM, Unisense, A.S.,  
148 Denmark) was used during EP and pH measurements. To exclude turbulence-induced variations in the  
149 potential of the reference electrode during EP profiling, a silicon tube filled with foam was mounted  
150 on the tip of the reference electrode.

### 151 **2.3. Solute Flux Measurements**

152            Solute flux incubations were performed for NH<sub>4</sub><sup>+</sup>, Fe<sup>2+</sup>, Mn<sup>2+</sup>, Ca<sup>2+</sup>, HPO<sub>4</sub><sup>2-</sup> and H<sub>4</sub>SiO<sub>4</sub>. At  
153 each time point, one core was placed outside the aquarium, and the isolated volume of overlying  
154 water in the core was continuously aerated. Parafilm was wrapped on top of the cores to prevent  
155 evaporation. Water samples of 3 mL were retrieved at 7 time points over 24 hours. The same volume  
156 of fresh artificial seawater was added to the cores directly after taking each sample. The samples were



157 filtered (0.45  $\mu\text{m}$ ), and subsamples were taken for ammonium (1 mL) and for metals (1 mL; acidified  
158 with 10  $\mu\text{L}$  Suprapur® HCl (35%) per mL sample), which were stored at  $-20^{\circ}\text{C}$  and  $4^{\circ}\text{C}$  respectively  
159 until further analysis.

#### 160 **2.4. Pore Water and Sediment Collection**

161 At each time point, two cores were sectioned at 0.5-1 cm resolution with an UWITEC push-  
162 up pole in a nitrogen-purged glovebag, but only samples for one core were used for sediment and pore  
163 water collection and analyses. Bottom water samples were retrieved from the overlying water in the  
164 cores. Slices for each depth interval were centrifuged at 3500 rpm for 20 minutes for pore water  
165 retrieval. Samples (1 mL) for  $\text{NH}_4^+$  were taken and stored at  $-20^{\circ}\text{C}$  until analysis. Samples (1 mL) for  
166 pore water S, Fe, Mn, Ca, P and Si were also collected and acidified with 10  $\mu\text{L}$  Suprapur® HCl  
167 (35%) per mL sample, which were stored at  $4^{\circ}\text{C}$  until analysis. Centrifuged sediment samples were  
168 freeze-dried and ground to a fine powder in a nitrogen-purged glovebox under a strictly anoxic  
169 environment to prevent oxidation (Kraal et al. 2009; Kraal and Slomp 2014). Only the top 5 cm of the  
170 solid-phase samples were analysed in further detail. The porosity (Supporting Information 1.1; Table  
171 S1) was calculated from the weight loss upon freeze-drying, using a sediment density of  $2.65 \text{ g cm}^{-3}$   
172 (Burdige 2006). Salt corrections were performed on the solid-phase data using the gravimetric water  
173 content and salinity to determine the amount of salt after freeze-drying.

#### 174 **2.5. Chemical Analysis of the Water and Sediment**

175 Concentrations of  $\text{NH}_4^+$  in the pore water and solute flux samples were determined using the  
176 phenol hypochlorite method (Koroleff 1969). The total Fe, Mn, Ca, P and Si concentrations (which  
177 are assumed to represent  $\text{Fe}^{2+}$ ,  $\text{Mn}^{2+}$ ,  $\text{Ca}^{2+}$ ,  $\text{HPO}_4^{2-}$  and  $\text{H}_4\text{SiO}_4$ ) in the pore water and solute flux  
178 samples were determined using Inductively Coupled Plasma-Optical Emission Spectroscopy (ICP-  
179 OES, Spectro Arcos). Dissolved Fe and Mn are assumed to be present in the form of  $\text{Fe}^{2+}$  and  $\text{Mn}^{2+}$ ,  
180 however some  $\text{Mn}^{3+}$  (Madison et al. 2013) or colloidal and nanoparticulate Fe and Mn might also be  
181 available (Boyd and Ellwood 2010; Raiswell and Canfield 2012). Concentrations of P and S are  
182 assumed to represent  $\text{HPO}_4^{2-}$  and  $\text{SO}_4^{2-}$  respectively. The colourimetric detection limit for  $\text{NH}_4^+$  was



183 0.5  $\mu\text{M}$ . The practical detection limit on the ICP-OES for Fe, Mn and P was 0.73, 0.11 and 7.30  $\mu\text{M}$ ,  
184 respectively.

185 Solid-phase Fe was fractionated into [1] labile ferric Fe (hydr)oxides and ferrous Fe ( $\text{FeS} +$   
186  $\text{FeCO}_3$ ), [2] crystalline Fe minerals, [3] magnetite and [4] pyrite (Supporting Information 1.2; Table  
187 S2), using a combination of two operational extraction methods (Poulton and Canfield 2005; Claff et  
188 al. 2010) as described by Kraal et al. (2017). Concentrations of Fe in all extracts were determined  
189 using the colourimetric phenanthroline method (APHA 2005). Solid-phase S was separated into [1]  
190 acid volatile sulphur (AVS; representing  $\text{FeS}$ ) and [2] chromium reducible sulphur (CRS; representing  
191  $\text{FeS}_2$ ; Table S1) using the method after Burton et al. (2006; 2008) as modified by Kraal et al. (2013).  
192 Sulphide released during the S extraction was trapped as  $\text{ZnS}$  in alkaline Zn acetate traps.  
193 Concentrations of S were determined by iodometric titration (APHA 2005). Solid-phase siderite  
194 ( $\text{FeCO}_3$ ) was determined by subtracting AVS from the labile ferrous concentrations retrieved from the  
195 first step of the Fe extraction. Solid-phase P was fractionated into [1] exchangeable P, [2] citrate-  
196 dithionite-bicarbonate (CDB)-P, [3] authigenic P, [4] detrital P and [5] organic P (Table S2) after  
197 Ruttenberg (1992) as modified by Slomp et al. (1996). The sum of exchangeable P and CDB-P  
198 represents metal bound P, as described in Hermans et al. (2019b). Concentrations of P in all extracts,  
199 except CDB, were measured with the molybdenum blue colourimetric method (Murphy and Riley  
200 1958). The P, Mn (assuming to represent Mn oxides; Hermans et al. 2019b) and Si (assuming to  
201 represent metal oxide bound Si; Kostka and Luther III 1994; Rao et al. 2016) in CDB extracts was  
202 determined using ICP-OES.

## 203 **2.6. Elemental Mapping of Fe, Mn, P and Ca**

204 On day 47, an undisturbed core (first 7 cm of surface sediment) was sampled for epoxy resin  
205 embedding for high-resolution elemental mapping (Jilbert et al. 2008; Jilbert and Slomp 2013). The  
206 epoxy-embedded core was split vertically using a rock saw. The surface was smoothed by applying a  
207 0.3  $\mu\text{m}$  alumina powder layer. Elemental maps of Fe, Mn, P and Ca (30  $\mu\text{m}$  resolution) were retrieved  
208 using a Desktop EDAX Orbis  $\mu\text{XRF}$  analyser (Rh tube set at 30 kV, 500  $\mu\text{A}$ , 300 ms dwell-time,  
209 equipped with a poly-capillary lens). Similar  $\mu\text{XRF}$  maps for Fe, Mn and P in epoxy embedded





210 surface sediment were obtained for two field sites: (1) the Gulf of Finland, for sediments collected in  
211 June 2016 as described by Hermans et al. (Submitted), and Lake Grevelingen, for sediments collected  
212 in January and May 2012 as described in Sulu-Gambari et al. (2016a; 2018).

### 213 **2.7. Fluorescence *In-situ* Hybridisation**

214 Fluorescence *in-situ* hybridisation (FISH; Pernthaler et al. 2001) was used to microscopically  
215 quantify the abundance of cable bacteria filaments, as described in Seitaj et al. (2015). FISH analysis  
216 was performed on one intact sediment core retrieved at our sampling site, and the sediment cores from  
217 our incubation experiment used for pore water collection at three time points (days 5, 26 and 207).  
218 These cores were sectioned at 0.5 cm depth resolution for the first 2.5 cm. Each sediment slice was  
219 homogenised and fixed with 0.5 mL ethanol ( $\geq 99.8\%$  purity), and stored in a 2 mL Eppendorf tube at  
220  $-20\text{ }^{\circ}\text{C}$ . For FISH analysis, a volume of 100  $\mu\text{L}$  was retrieved from the Eppendorf tubes and mixed  
221 with a 1:1 solution of PBS/ethanol (500  $\mu\text{L}$ ). Then 10  $\mu\text{L}$  of this mixture was filtered through a  
222 polycarbonate membrane (type GTTP; pore size 0.2  $\mu\text{m}$ , Millipore, USA). Cable bacteria were  
223 classified with a *Desulfobulbaceae*-specific oligonucleotide probe (DSB706; 5-ACC CGT ATT CCT  
224 CCC GAT-3') after counter staining with DAPI (1  $\mu\text{g}/\text{mL}$ ) under an epifluorescence microscope  
225 (Zeiss Axioplan, Germany) at 100x magnification. The abundance of cable bacteria was quantified by  
226 determining the length and diameter of all observed filaments in a field ( $105 \times 141\ \mu\text{m}$ ) on the filter at  
227 100x magnification (200 fields per sample). Cable bacterial abundances are expressed as filament  
228 length per volumetric unit ( $\text{m cm}^{-3}$ ) or depth integrated per unit area of sediment surface ( $\text{m cm}^{-2}$ ),  
229 consistent with previous studies (Schauer et al. 2014; Malkin et al. 2017).

### 230 **2.8. Scanning Electron Microscopy**

231 Cable bacteria filaments were taken from surface sediments from the oxic zone (upper 2 mm)  
232 after 40 days using a microscope and were transferred to a 15 mL centrifuge tube. The tube was filled  
233 to a volume of  $\sim 10\ \text{mL}$  using ultra clean water, and was subsequently centrifuged at 2100 rpm for 2  
234 min, after which the water was discarded. This washing step was repeated three times. The washed  
235 samples were then transferred to a sample stub, where the sediment was air-dried over-night prior to  
236 gold coating. The filaments were subsequently subjected to scanning electron microscopy (SEM)



237 imaging on a Phenom ProX Desktop SEM (Phenom-World B.V., the Netherlands) to obtain high-  
238 resolution images, as described in Geerlings et al. (2019). SEM images were generated under 0.1-0.3  
239 mbar vacuum, and a high accelerating voltage (10 or 15 kV).

## 240 **2.9. Data Analysis and Calculations**

241 The diffusive uptake of O<sub>2</sub> was calculated from the high-resolution O<sub>2</sub> depth profiles using the  
242 PROFILE software package (Berg et al. 1998). Total H<sub>2</sub>S ( $\Sigma\text{H}_2\text{S} = \text{H}_2\text{S} + \text{HS}^- + \text{S}^{2-}$ ) was calculated as  
243 a function of the recorded H<sub>2</sub>S and pH values, accounting for temperature and salinity (Millero et al.  
244 1988; Jeroschewski et al. 1996).

245 The EP depth profiles were normalised by subtracting the background EP signal in the  
246 overlying water from the EP depth profiles, to calculate the EP value relative to that in the overlying  
247 water (Damgaard et al. 2014). The electric field in the sediment was calculated from the linear slope  
248 of the EP depth profiles (average of triplicates) in the surface sediments (Risgaard-Petersen et al.  
249 2014). The magnitude of the current density was subsequently calculated from the gradient in the EP,  
250 the so-called electric field, using Ohm's law:

$$J = \sigma_{sed} \cdot E \quad (1)$$

251 where  $J$  represents the magnitude of the current density (mA m<sup>-2</sup>),  $\sigma_{pw}$  is the conductivity of  
252 the sediment matrix (S m<sup>-1</sup>) and  $E$  (mV m<sup>-1</sup>) represents the electric field. The conductivity of the pore  
253 water was corrected for tortuosity and calculated as a function of the temperature and salinity using  
254 the equations provided by Fofonoff and Millard Jr (1983).

255 The solute fluxes were calculated as described in Glud (2008) and Rao et al. (2016):

$$J = \frac{\Delta C_{ow}}{\Delta t} \cdot \frac{V_{ow}}{A} \quad (2)$$

256 where  $J$  represents the diffusive flux (mmol m<sup>-2</sup> d<sup>-1</sup>),  $\Delta C_{ow}$  represents the concentration change in the  
257 overlying water (mmol m<sup>-3</sup>),  $\Delta t$  is the incubation time (d),  $V_{ow}$  is the volume in the overlying water  
258 (m<sup>3</sup>) and  $A$  the surface area of sediment in the core (m<sup>2</sup>). In our experimental setup, only those fluxes  
259 were measurable for NH<sub>4</sub><sup>+</sup>, Fe<sup>2+</sup>, Mn<sup>2+</sup> and HPO<sub>4</sub><sup>2-</sup>, that were >0.08, >0.06, >0.01 and >0.55 mmol m<sup>-2</sup>



260  $d^{-1}$ , respectively. However, for these four solutes, fluxes were always too low to be detected. Hence,  
261 only  $Ca^{2+}$  and  $H_4SiO_4$  fluxes are presented.

262 Diffusive downward fluxes of  $SO_4^{2-}$  and diffusive upward fluxes of  $NH_4^+$ ,  $Fe^{2+}$ ,  $Mn^{2+}$  and  
263  $Ca^{2+}$  were calculated from linearized pore water gradients using Fick's first law (Berner 1980):

$$J = -\phi D_s \cdot \frac{dC}{dz} \quad (3)$$

264

265 The molecular diffusion coefficient was calculated as a function of pressure, salinity and  
266 temperature using the R package *marelac* (Soetaert et al. 2010) and corrected for the ambient  
267 tortuosity using the relations listed in Boudreau (1997).

## 268 3. RESULTS

### 269 3.1. Abundance of Cable Bacteria

270 Examination of the top 2.5 cm of the surface sediments using FISH showed the presence of  
271 filamentous cable bacteria (Fig. 1C; Fig. S1). The *in-situ* cable bacterial abundance in the sediment at  
272 our field site was low ( $14 \text{ m cm}^{-2}$ ). However, after 5 days of incubation in the laboratory, the  
273 abundance increased strongly ( $724 \text{ m cm}^{-2}$ ). At day 26 the abundance of cable bacteria was even  
274 higher ( $1035 \text{ m cm}^{-2}$ ). After 207 days, the cable bacterial abundance in the surface sediment was low  
275 again ( $131 \text{ m cm}^{-2}$ ). SEM imaging confirmed that filaments were indeed cable bacteria (Fig. 1D), as  
276 the external surface of the filament was characterised by a parallel pattern of ridges and grooves along  
277 its latitudinal axis, which is a typical feature of cable bacteria (Cornelissen et al. 2018; Geerlings et al.  
278 2019).

### 279 3.2. High-resolution Depth Profiles of pH, $O_2$ , $\Sigma H_2S$ and EP

280 High-resolution depth profiles of pH showed the development of a distinct peak near the  
281 sediment-water interface at day 5, and acidification of the pore water in the deeper sediment (Fig.  
282 2A). The width of this pore water acidification zone increased with time and reached its maximum at



283 day 26, followed by a decrease in the acidification. The distinct pH peak near the sediment-water  
284 interface gradually disappeared after 33 days. The depth of O<sub>2</sub> penetration in the sediment remained  
285 constant within the first 40 days of incubation (~1.1 mm) and subsequently moved downwards with  
286 time to 9.6 mm (Fig. 2A; Fig. 3; Fig. S2). The dissolved ΣH<sub>2</sub>S concentrations remained low (<5 μM)  
287 throughout the experiment (Fig. 2A). The ΣH<sub>2</sub>S appearance depth was initially equivalent to the O<sub>2</sub>  
288 penetration depth, and shifted downwards within 5 days, creating a suboxic zone where O<sub>2</sub> and ΣH<sub>2</sub>S  
289 remained below detection (Fig. 2A; Fig. 3). The width of the suboxic zone remained relatively  
290 constant with time (~25 mm; Fig. 3), and only slight decreased after 207 days.

291 The EP depth profiles indicate a rapid establishment of an electric current after 5 days (0.4  
292 mV; Fig. 2B). The time-series of depth profiles show that the EP increased and also accumulated over  
293 a thicker depth horizon. At day 26 the EP reached its maximum value (1.2 mV), followed by a  
294 decrease with time. Long-distance electron transport was not active in the anoxic control core (Fig.  
295 S3).

### 296 3.3. Diffusive Uptake of O<sub>2</sub> and Current Density

297 The diffusive O<sub>2</sub> uptake of the sediment was highest after 5 days and gradually decreased  
298 with time from ~30 to ~3.6 mmol m<sup>-2</sup> d<sup>-1</sup> (Fig. 4A). The current density rapidly increased from day 0  
299 to day 18, from 6 to 128 e<sup>-</sup> mmol m<sup>-2</sup> d<sup>-1</sup>, and then gradually decreased with time (Fig. 4B). The  
300 duplicate measurements show the same trend for the diffusive O<sub>2</sub> uptake and the current density,  
301 which indicates that the results are reproducible.

### 302 3.4. Pore Water Profiles

303 Concentrations of NH<sub>4</sub><sup>+</sup> were low near the sediment-water interface and increased with  
304 sediment depth reaching maximum levels of up to 1.7 mM at depth in the sediment (Fig. 5). The time-  
305 series suggest a gradual decrease in production of dissolved NH<sub>4</sub><sup>+</sup> in the sediment leading to  
306 decreasing concentrations with time. The pore water depth profiles of dissolved SO<sub>4</sub><sup>2-</sup> show a decline  
307 with sediment depth at all time points. However, SO<sub>4</sub><sup>2-</sup> concentrations remained relatively constant  
308 within the top 2 cm of surface sediment between day 12 and 33. Dissolved Fe<sup>2+</sup>, Mn<sup>2+</sup> and Ca<sup>2+</sup> all



309 show the development of distinct peaks in the pore water with time, and after 40 days those peaks  
310 disappear again. Pore water concentrations of  $\text{HPO}_4^{2-}$  generally increased with sediment depth for all  
311 time points, and concentrations within the top 2 cm were below the detection limit indicating removal.  
312 Dissolved  $\text{H}_4\text{SiO}_4$  increased with sediment depth reaching concentration of up to 1 mM.

### 313 3.5. Diffusive Fluxes

314 Calculated diffusive fluxes of  $\text{NH}_4^+$  into the oxic zone decreased during the incubation  
315 experiment from 4.7 to 1.8  $\text{mmol m}^{-2} \text{d}^{-1}$  (Fig. 6A; Fig. S4; Table S3). Rates of  $\text{SO}_4^{2-}$  reduction  
316 estimated from the linear gradient of the decrease in pore water  $\text{SO}_4^{2-}$  in the surface sediment with  
317 depth generally also showed a decrease with time (Fig. 6B; Fig. S5; Table S3). The upward diffusive  
318 flux of  $\text{Fe}^{2+}$  greatly increased from day 5 to day 12 and then gradually decreased with time (Fig 6C;  
319 Fig. S6; Table S3). The upward diffusive flux of Mn showed an increase in the initial stage of the  
320 experiment and reached its maximum at day 18, followed by a decrease with time (Fig. 6D; Fig. S7;  
321 Table 3). The upward diffusive flux of  $\text{Ca}^{2+}$  showed no clear trend with time, however after 207 days  
322 the flux became extremely low (Fig. 6E; Fig. S8). The upward diffusive flux of  $\text{H}_4\text{SiO}_4$  also showed  
323 an increase in the initial stage of the experiment, and reached its maximum at day 12, followed by a  
324 decrease with time (Fig. 6F; Fig. S9).

### 325 3.6. Solid-phase Profiles

326 The surface sediment in the oxic cores became more enriched in Fe oxides with time, with  
327 concentrations increasing from 53 to 485  $\mu\text{mol g}^{-1}$  (Figure 7). The deeper sediment in the oxic cores  
328 and the entire anoxic control core had low or no Fe oxides. At day 5, FeS was strongly depleted  
329 within the top 1 cm of the surface sediment and was gradually lost further with time. At day 621, most  
330 of the FeS within the top 2.5 cm of the surface sediment had been dissolved. The anoxic core did not  
331 show such a depletion of FeS in the surface sediment and even showed a slight increase in FeS. Solid-  
332 phase siderite remained rather constant with depth from day 5 to 33, but afterwards was gradually lost  
333 from the surface sediment. At day 621 a large proportion of the siderite was dissolved within the top 2  
334 cm. Solid-phase siderite concentrations remained constant with depth in the anoxic control core.



335 Solid-phase depth profiles of Mn oxides, metal bound P and metal oxide bound Si all showed a  
336 gradual increase in the surface sediment with time.

### 337 **3.7. High-resolution Elemental Mapping**

338 High-resolution desktop  $\mu$ XRF mapping of Fe, Mn, P and Ca of our core after 47 days of  
339 incubations revealed a subsurface sediment layer highly enriched in Fe and P (Fig. 8A). Subsurface  
340 enrichments in Fe, P and Mn in relatively thin layers were also observed in sediments populated by  
341 cable bacteria in the Gulf of Finland and Lake Grevelingen (Fig. 8B and C). In the latter system, the  
342 layers enriched in Fe, P, Mn broadened upon recolonization by macrofauna (Fig. 8D).

## 343 **3. DISCUSSION**

### 344 **4.1. Metabolic Activity of Cable Bacteria**

345 Cable bacteria in our incubation experiment demonstrated a rapid growth, since their  
346 abundance greatly increased after 5 days, and reached its peak at day 26 (Fig 1C). Such high  
347 abundances are similar to those observed in previous experiments, in which FeS-rich marine  
348 sediments from Aarhus Bay and Lake Grevelingen were incubated (Schauer et al. 2014; Burdorf et al.  
349 2018). The activity of cable bacteria exerted a strong impact on the pore water depth profiles of pH,  
350  $O_2$ , and  $\sum H_2S$ , as evident from the development of a pH maximum near the sediment-water interface,  
351 the strong pore water acidification in the deeper sediment and the development of a suboxic zone (Fig.  
352 2A). These pore water depth profiles resemble the distinct biogeochemical fingerprint typical for  
353 active cable bacteria, as observed in previous laboratory incubation experiments (Risgaard-Petersen et  
354 al. 2012; Malkin et al. 2014; Schauer et al. 2014; Vasquez-Cardenas et al. 2015; Rao et al. 2016;  
355 Burdorf et al. 2018). The widening of the suboxic zone with time (Fig 3) is a consequence of the  
356 downward expansion of the cable bacteria filament network (Schauer et al. 2014; Vasquez-Cardenas  
357 et al. 2015).

358 The EP depth profiles demonstrated that long-distance electron transport by cable bacteria  
359 was already active 5 days after the start of the experiment, as indicated by the increase of EP at depth  
360 to 0.4 mV). With time, the EP signal increased to higher values and also accumulated over a thicker



361 depth horizon (Fig. 2B), indicating that cable bacteria activity both increased and extended to deeper  
362 sediment depth, which is also a consequence of the downward expansion of cable bacteria filaments.  
363 The EP reached a maximum after 18 days (1.3 mV; Fig. 2B) in concert with the highest current  
364 density of  $\sim 130 \text{ mmol e}^- \text{ m}^{-2} \text{ d}^{-1}$  (Fig 4B). This maximum EP value and current density are similar in  
365 magnitude to those found in sediment incubations with seawater with a similar salinity (Damgaard et  
366 al. 2014). From day 18 onwards the EP and current density flux gradually decreased with time to 13  
367  $\text{mmol e}^- \text{ m}^{-2} \text{ d}^{-1}$  after 207 days (Fig. 4B), which implies a decrease in the metabolic activity of cable  
368 bacteria. The suboxic zone persisted long after the current density had decreased (Fig. 3).

369 To summarise, the metabolic activity of cable bacteria was likely highest between day 18 and  
370 day 26 based on the cable bacterial abundances, the extent of acidification of the pore water and the  
371 current density (Fig 1C; Fig 2A and Fig 4B).

#### 372 4.2. Organic Matter Degradation

373 Ammonium fluxes are assumed to reflect rates of anaerobic degradation of organic matter (Fig.  
374 5), and the observed decline during the experiment coincides with the decrease in activity of cable  
375 bacteria based on the EP profiles and current density (Fig. 2B; Fig 4B). This suggests that the  
376 availability of easily degradable organic matter plays a role in sustaining the metabolic activity of  
377 cable bacteria, most likely by controlling the rate of  $\text{SO}_4^{2-}$  reduction (Nielsen and Risgaard-Petersen  
378 2015).

379 Rates of  $\text{SO}_4^{2-}$  reduction estimated from the linear gradient of the decrease in pore water  $\text{SO}_4^{2-}$  in  
380 the surface sediment with depth indeed also showed a decline during the experiment. We note,  
381 however, that a direct measurement of  $\text{SO}_4^{2-}$  reduction rates (Fossing and Jørgensen 1989; Kallmeyer  
382 et al. 2004) would provide a better indicator, because  $\text{SO}_4^{2-}$  estimated from pore water profiles are in  
383 general lower than rates estimated from tracer experiments (Hermans et al. 2019a; Sandfeld et al.  
384 2020). Another cause for a slight underestimation of our  $\text{SO}_4^{2-}$  reduction rates, is due to the effect of  
385 the electric field imposed by cable bacteria, which is not taken into account in Fick's law.



386 The metabolic activity of cable bacteria can lead to the production of  $\text{SO}_4^{2-}$  in the suboxic zone  
387 via anodic sulphide oxidation (Risgaard-Petersen et al. 2012; Rao et al. 2016). We suspect that this  
388 also explains the lack of change in pore water  $\text{SO}_4^{2-}$  with depth in the upper 2 cm of the sediment in  
389 our experiment between 12 and 40 days (Fig. 5). Despite relatively high  $\text{SO}_4^{2-}$  reduction rates ranging  
390 from 5.4 to 17.6  $\text{mmol m}^{-2} \text{d}^{-1}$  (Fig. 6B; Table S3), pore water concentrations of  $\Sigma\text{H}_2\text{S}$  remained very  
391 low throughout the experiment (Fig. 2A). This is likely due to the direct consumption of  $\Sigma\text{H}_2\text{S}$   
392 through the activity of cable bacteria, preventing  $\Sigma\text{H}_2\text{S}$  from accumulating in the pore water, or  
393 alternatively, precipitation of FeS by dissolved  $\text{Fe}^{2+}$  released from the dissolution of siderite.

394 Laboratory experiments have shown that S-oxidation by cable bacteria can play a dominant role  
395 in the  $\text{O}_2$  uptake of coastal sediments (Nielsen et al. 2010; Schauer et al. 2014; Nielsen and Risgaard-  
396 Petersen 2015), and model analysis predicts up to 93% of the total  $\text{O}_2$  uptake (Meysman et al. 2015).  
397 When we plot diffusive uptake of  $\text{O}_2$  against the current density (i.e. upward flux of electrons towards  
398 the oxic zone), a linear relationship – with some scatter - emerges for days 12 to 621 (Fig. 9).  
399 However, the data points for day 0 and 5 during the initial stages of our experiment do not follow this  
400 linear relationship. We explain these findings as follows: At day 0, the cable bacteria were not active  
401 yet and other processes, such as aerobic respiration and oxidation of  $\text{NH}_4^+$  and other solutes (Table 2)  
402 and solids (FeS) dominated the consumption of  $\text{O}_2$ . At day 5 and 12, the activity of cable bacteria and  
403 the oxidation of reduced products from anaerobic degradation of organic matter both contributed to  
404 consumption of  $\text{O}_2$ . From day 12 onwards, both the  $\text{O}_2$  consumption and electron flux follow a  
405 downward decrease with time (Fig. 9). If cable bacteria would account for all of the  $\text{O}_2$  consumption,  
406 a ratio between the diffusive uptake of  $\text{O}_2$  and the current density of 1:4 is expected (Fig. 1A; Nielsen  
407 et al. 2010). We find that from day 12 onwards, most data points plot rather close to the line for this  
408 1:4 relationship (Fig. 9), suggesting that cathodic  $\text{O}_2$  reduction by cable bacteria is responsible for  
409 nearly all  $\text{O}_2$  consumption in the sediment (in line with the model results of Meysman et al. 2015).  
410 This however poses a problem for the nitrogen budget, because our data indicate complete removal of  
411 the  $\text{NH}_4^+$  that diffuses upward into the oxic zone (Fig. 6A), and based on the solute fluxes, no escape  
412 to the overlying water (see section 2.4). This implies substantial  $\text{O}_2$  consumption due to nitrification





413 (Table 2). These findings can be explained, however, if we assume that the  $\text{NO}_3^-$  that is being formed  
414 near the sediment-water interface is also used for the metabolic activity of cable bacteria. It has been  
415 shown that cable bacteria can couple the oxidation of  $\Sigma\text{H}_2\text{S}$  to  $\text{NO}_3^-$  in the absence of  $\text{O}_2$  (Marzocchi  
416 et al. 2014). Our data suggest that this process may also occur in sediments where  $\text{O}_2$  is present in  
417 concert with  $\text{NO}_3^-$  near the sediment-water interface. Another explanation is that cable bacteria might  
418 consume  $\text{O}_2$  directly above the sediment-water interface, as recently has been proposed by Burdorf et  
419 al. (2018). Lastly, the current density might be slightly overestimated, since it ignores other sources  
420 that can create an electric potential, such as the diffusion potential (Revil et al. 2012; Nielsen and  
421 Risgaard-Petersen 2015).

#### 422 **4.3. Impact of Cable Bacteria on Fe, Mn and S Cycling**

423 The activity of cable bacteria had a strong impact on the biogeochemistry of the surface sediment  
424 in our experiment (Fig. 7). Cable bacteria activity induced an intense acidification of the pore water in  
425 the suboxic zone (Fig 2A), which led to the dissolution of Fe and Mn minerals in deeper sediment  
426 layers, as can be inferred from the sharp maxima in dissolved  $\text{Fe}^{2+}$  and  $\text{Mn}^{2+}$  in the pore water  
427 reaching concentrations of up to  $\sim 1700$  and  $\sim 80$   $\mu\text{M}$ , respectively (Fig. 5). The twenty-fold higher  
428 dissolved  $\text{Fe}^{2+}$  concentrations with respect to pore water  $\text{Mn}^{2+}$  can be attributed to the relatively higher  
429 availability of FeS and siderite compared to the availability of Mn carbonates in the sediment that was  
430 used for incubation (Lenstra et al. 2020). The peaks in dissolved  $\text{Fe}^{2+}$  and  $\text{Mn}^{2+}$  in the pore water  
431 broadened over time spanning a depth of  $>5\text{cm}$  (Fig. 5; Fig. S6; Fig. S7).

432 The upward diffusive flux of dissolved  $\text{Fe}^{2+}$  and  $\text{Mn}^{2+}$  was highest after 12 days, reaching values  
433 of up to  $3.16$  and  $0.16$   $\text{mmol m}^{-2} \text{d}^{-1}$  respectively. Fluxes subsequently gradually decreased with time  
434 (Fig. 6C and D). The continuous upward diffusion of dissolved  $\text{Fe}^{2+}$  and  $\text{Mn}^{2+}$  led to enrichments of  
435 poorly crystalline Fe and Mn oxides in the surface sediment (Fig. 7). Despite high upward fluxes of  
436 dissolved  $\text{Fe}^{2+}$  and  $\text{Mn}^{2+}$  towards the sediment-water interface, our solute flux incubations indicate  
437 there was little escape of  $\text{Fe}^{2+}$  and  $\text{Mn}^{2+}$  to the overlying water (see section 2.4). This implies that all  
438  $\text{Fe}^{2+}$  and  $\text{Mn}^{2+}$  that diffused upward was precipitated as Fe and Mn oxides upon contact with  $\text{O}_2$  or  
439  $\text{NO}_3^-$  (Buresh and Moraghan 1976; Kuz'minskii et al. 1994; Straub et al. 1996). Little or no escape of



440 dissolved  $\text{Fe}^{2+}$  from the sediment into the overlying water, was suggested previously for a field site  
441 with active cable bacteria based on diffusive flux calculations (Lake Grevelingen; Sulu-Gambari et al.  
442 2016a) and was determined in flux incubations of cores during a laboratory experiment with cable  
443 bacteria (Rao et al. 2016).

444 At the start of the experiment, the sedimentary FeS content was ( $\sim 25 \mu\text{mol g}^{-1}$ ), which is not  
445 unusual for coastal sediments on the north-western Black Sea margin (Wijsman et al. 2001), but is  
446 low compared to sediments in eutrophic coastal systems (e.g. Morgan et al. 2012; Kraal et al. 2013;  
447 Hermans et al. 2019a). The solid-phase depth profiles reveal a gradual removal of the FeS in the  
448 surface sediment in our experiment over time (Fig. 7). At the end of our experiment (621 days), there  
449 was no longer any FeS within the top 1.5 cm of the sediment. While approximately  $90 \text{ mmol m}^{-2}$  of  
450 FeS was removed from the surface sediment within the first 5 days, a total of  $\sim 240 \text{ mmol m}^{-2}$  was  
451 removed after 621 days (Fig. 10; Table 3). Likely, part of the FeS that was removed from the surface  
452 sediment within the first 5 days was removed through oxidation upon contact with  $\text{O}_2$ , rather than the  
453 metabolic activity of cable bacteria itself. The pore water acidification associated with cable bacteria  
454 activity led to a strong loss of siderite within the top 2 cm of the sediment, with a total removal of  
455  $\sim 560 \text{ mmol m}^{-2}$  during the experiment (Fig. 7; Fig. 10; Table 3). The depletion of sedimentary FeS  
456 and siderite was directly proportional to the formation of Fe oxides near the sediment-water interface  
457 (Fig. 10), and accounted for 30% and 70% of the Fe oxides, respectively (Table 3).

458 With these data we cannot accurately determine the role of FeS versus  $\text{SO}_4^{2-}$  reduction in  
459 supplying the  $\sum\text{H}_2\text{S}$  sustaining the activity of cable bacteria throughout the experiment. This is  
460 primarily related to the variability between cores, and for this type of calculation, the low temporal  
461 resolution of sampling. However, we can make an estimation of the relative role of  $\text{SO}_4^{2-}$  reduction  
462 and FeS dissolution in  $\sum\text{H}_2\text{S}$  production, based on the pore water profiles of  $\text{SO}_4^{2-}$  and dissolved  $\text{Fe}^{2+}$ ,  
463 and the solid-phase mass balance of FeS and siderite (Fig. 6B and C; Table 4). This estimation shows  
464 that  $\text{SO}_4^{2-}$  was mainly responsible for  $\sum\text{H}_2\text{S}$  production, accounting for 85-99% (Table 4), and thus  
465 that the dissolution of FeS only played a minor role in providing  $\sum\text{H}_2\text{S}$ .



466 **4.4. Impact of Cable Bacteria on Ca, P and Si Cycling**

467 Cable bacteria activity is known to lead to dissolution of Ca carbonates, because of the strong  
468 acidification of the pore water (Risgaard-Petersen et al. 2012; Rao et al. 2016). We indeed find similar  
469 maxima in pore water  $\text{Ca}^{2+}$  during the experiment (Fig. 5) and a high upward flux of  $\text{Ca}^{2+}$  (up to ~18  
470  $\text{mmol m}^{-2} \text{d}^{-1}$ ; Fig. 6E; Fig. S8) of which a substantial fraction (up to ~55%) escapes to the overlying  
471 water (Fig. S10; Table S4), which is consistent with a previous incubation experiment Rao et al.  
472 (2016).

473 Pore water depth profiles of  $\text{HPO}_4^{2-}$  reveal a production at depth and removal of all upward  
474 diffusing  $\text{HPO}_4^{2-}$  within the first 1-3 cm of the surface sediment (Fig. 5). A major proportion of this  
475  $\text{HPO}_4^{2-}$  is bound to Fe oxides (Fig. 7). Given that a large proportion of the Fe oxides in our sediment  
476 cores derive from the dissolution of siderite, this suggests that the buffer mechanism that delays the  
477 benthic release of  $\text{HPO}_4^{2-}$  through retention of P associated with newly formed Fe oxides (Sulu-  
478 Gambari et al. 2016b), might also be active in systems that are relatively poor in sedimentary FeS.

479 The shape of the pore water  $\text{HPO}_4^{2-}$  profiles suggests that some of the  $\text{HPO}_4^{2-}$  is removed below  
480 the zone where Fe and Mn oxides are present (Fig. 5; Fig. 7). A possible explanation could be the  
481 formation of vivianite, an Fe(II) phosphate mineral. Vivianite formation in sediments typically occurs  
482 when pore water levels of  $\text{Fe}^{2+}$  and  $\text{HPO}_4^{2-}$  are high and concentrations of  $\Sigma\text{H}_2\text{S}$  are low (Nriagu  
483 1972), as observed in our study. In our experiment, free  $\Sigma\text{H}_2\text{S}$  does not accumulate in the pore water,  
484 which we attribute to removal through the activity of cable bacteria and FeS formation at depth (Fig.  
485 2A; Fig. 7). Hence, cable bacteria may create a geochemical niche that allows the formation of  
486 vivianite in the suboxic zone. Further work with sediments with higher P concentrations would be  
487 needed to assess this with direct measurement techniques, such as X-ray spectroscopy (Egger et al.  
488 2015; Kraal et al. 2017; Sulu-Gambari et al. 2018). Other sediment P pools, i.e. organic, authigenic  
489 and detrital P remained constant over time, indicating that the P contents determined for discrete  
490 sediment slices using sequential extractions were not affected by pore water acidification as a result of  
491 cable bacteria activity (Table S5).



492 Pore water  $\text{H}_4\text{SiO}_4$  profiles show a typical increase with depth as observed upon dissolution of  
493 biogenic silica in marine sediments (Aller 2014). Fluxes of  $\text{H}_4\text{SiO}_4$  towards the sediment-water  
494 interface range up to  $\sim 2.8 \text{ mmol m}^{-2} \text{ d}^{-1}$  and gradually decreased with time (Fig. 6F; Fig. S9). The  
495 results of the solute flux incubations indicate that most of this  $\text{H}_4\text{SiO}_4$  escaped to the overlying water  
496 (ranging from 28 to 92%; Table S4; Fig. S10). The decline in the benthic release flux of  $\text{H}_4\text{SiO}_4$   
497 contrasts with results of a previous incubation experiment by Rao et al. (2016) with similar pore water  
498 concentrations of  $\text{H}_4\text{SiO}_4$  reaching values up to  $\sim 1 \text{ mM}$ . In their study, the flux remained constant  
499 over time, possibly because of differences in the amount of biogenic Si in the sediment. The solid-  
500 phase metal oxide bound Si pool in the surface sediment increased directly proportional to the  
501 formation of Fe oxides throughout the experiment (Fig. 7). Silica is known to adsorb to Fe oxides  
502 (Sigg and Stumm 1981; Davis et al. 2002). Hence, the results suggest that the Fe oxides formed  
503 through the activity of cable bacteria captured some of the upward diffusing  $\text{H}_4\text{SiO}_4$ .

#### 504 **4.5. Sediment Marker for Cable Bacteria Activity**

505 Visual observations of core photographs reveal the gradual development of an orange layer (oxic  
506 zone) up to 9 mm thick, overlying a grey layer (suboxic zone) and a black layer (sulphidic zone)  
507 during the experiment (Fig. S11). This colour zonation is typical for sediments that have been  
508 geochemically affected by cable bacteria activity (Nielsen and Risgaard-Petersen 2015; Sulu-Gambari  
509 et al. 2016a). High-resolution elemental maps of our sediments reveal the development of a  $\sim 0.3 \text{ mm}$   
510 thin subsurface layer highly enriched in Fe oxides and associated P, 47 days after the start of the  
511 incubation (Fig. 8A). Below, we describe the formation of this layer in more detail and explain why  
512 such subsurface enrichments, detected with  $\mu\text{XRF}$ , may act as an additional sediment marker for  
513 present or recent cable bacteria activity, also in cases where visual observations are not conclusive.

514 During the experiment,  $\text{O}_2$  penetration varied within a narrow range and was initially fixed  
515 between 1 and 2 mm depth (Fig. 3A), with the layer highly enriched in Fe forming mostly at a depth  
516 of 2 mm (Fig. 8A). This can be explained by rapid oxidation of upward diffusing  $\text{Fe}^{2+}$  upon contact  
517 with  $\text{O}_2$  (and possibly  $\text{NO}_3^-$ ; Fig. 6C). Directly, above the Fe oxide layer a broader  $\sim 0.8 \text{ mm}$  thick Mn  
518 oxide layer was observed (Fig. 8A). This contrast in zonation between Fe and Mn is likely due to the



519 slower oxidation kinetics of  $\text{Mn}^{2+}$  compared to  $\text{Fe}^{2+}$  (Burdige 1993; Luther 2010; Learman et al.  
520 2011).

521 While the Fe oxide layer is clearly enriched in P, we also observed a second layer enriched in P  
522 close to the sediment-water interface (Fig. 8A). In this layer, P is strongly correlated with Ca. This  
523 layer likely consists of carbonate fluorapatite (CFA), a Ca-P mineral, which is typically formed in  
524 marine sediments (Van Cappellen and Berner 1988; Ruttenger and Berner 1993). Possibly, the high  
525 pore water pH near the sediment-water interface (resulting from cathodic  $\text{O}_2$  reduction by cable  
526 bacteria; Fig. 2A), promotes apatite formation (Bellier et al. 2006), and the elevated  $\text{Ca}^{2+}$   
527 concentrations (Fig. 5) created a biogeochemical niche for the formation of CFA.

528 Such focusing of Fe, Mn, P and associated elements within a thin subsurface layer, as a  
529 consequence of cable bacteria activity, also occurs in the field. This was demonstrated by Hermans et  
530 al. (Submitted) in a study of a coastal site in the Gulf of Finland where cable bacteria were recently  
531 active. Here,  $\mu\text{XRF}$  mapping of resin embedded sediments revealed strong focusing of Fe oxides,  
532 Mn(II) phosphates and Fe bound P within a 3 mm thick layer near the sediment-water interface (Fig.  
533 8B). A re-assessment of the  $\mu\text{XRF}$  data of Sulu-Gambari et al. (2016a; 2018) of surface sediments  
534 with active cable bacteria from seasonally hypoxic marine Lake Grevelingen in January also revealed  
535 similar subsurface enrichments in Fe, Mn and P (Fig. 8C). Importantly, no visual signals for cable  
536 bacteria based on the colour pattern of the sediment were observed at the time.

537 Macrofaunal activity likely counteracts or prevents strong focusing of Fe oxides and associated P  
538 within such a thin subsurface layer at field sites. Bioturbation, i.e. mixing of the sediment, typically  
539 leads to oxidation from the sediment surface downwards (Norkko et al. 2012). Bioirrigation can  
540 efficiently pump  $\text{O}_2$  into the pore water and thereby enhance the oxidation of dissolved  $\text{Fe}^{2+}$   
541 (Kristensen et al. 2012; Norkko et al. 2012), but is not expected to lead to such a sharp oxidation front  
542 (Norkko et al. 2012; Hermans et al. 2019a). This is also evident from high-resolution elemental maps  
543 of the surface sediment from Lake Grevelingen in May, which shows the disappearance of the thin



544 layer highly enriched in Fe and P formed by cable bacteria in January as a consequence of  
545 macrofaunal activity in May (Fig. 8D; Seitaj et al. 2015; Sulu-Gambari et al. 2016b).

546 We conclude that the focusing of Fe, Mn and associated P within a thin layer below the sediment-  
547 water interface is likely a consistent feature in sediments populated by active cable bacteria and may  
548 be a marker for their recent activity. When using standard techniques for sediment sampling (i.e. core  
549 slicing and chemical analysis of these slices), these layers may be missed due to the relatively coarse  
550 depth resolution. Hence,  $\mu$ XRF mapping of epoxy embedded sediment is recommended.

#### 551 **4.6. Cable Bacteria Activity at the Field Site**

552 We can only speculate about the possible *in-situ* relevance of cable bacteria at the coastal site  
553 in the western Black Sea where the sediment for our incubation was collected. At this site, both  
554 bivalves (up to  $\sim 7200$  ind.  $m^{-2}$ ) and polychaetes (up to  $\sim 1700$  ind.  $m^{-2}$ ) were observed at the time of  
555 sampling (Lenstra et al. 2019). Macrofauna can inhibit the activity of cable bacteria through  
556 bioturbation by physically cutting and damaging the filaments, rendering them unable to transport  
557 electrons (Malkin et al. 2014). Recent work has shown, however, that in some cases, cable bacterial  
558 communities can also thrive in sediments with macrofauna (Burdorf et al. 2017; Malkin et al. 2017;  
559 Aller et al. 2019). In a study of bivalve reefs, cable bacteria were found to efficiently remove highly  
560 toxic  $\Sigma H_2S$ , which is beneficial for bivalves (Malkin et al. 2017). Cable bacteria can also be abundant  
561 in bioturbated deposits, when associated with stable subdomains of the bioturbated zone, such as  
562 worm tubes (Aller et al. 2019). In such settings, a more complex precipitation pattern, e.g. along tube  
563 linings is observed (Aller et al. 2019), than described here for laboratory experiments with defaunated  
564 sediments and field sediments with an impoverished macrofaunal population (Fig. 8A). Further field  
565 studies are required to assess the role of cable bacteria at our field site, preferably including an  
566 assessment of the burrow structures.

#### 567 **Conclusions**

568 The results of our laboratory incubation (with a total duration of 621 days) highlight the  
569 strong impact of cable bacteria on Fe, Mn, P and S dynamics in coastal sediments. The strong acidity



570 of the pore water associated with the activity of cable bacteria, which was monitored using  
571 microsensor profiling of the EP during the experiment, led to dissolution of FeS and siderite and  
572 formation of Fe and Mn oxides and Ca-P in mineral form near the sediment surface. Both FeS and  
573  $\text{SO}_4^{2-}$  reduction provided the  $\sum\text{H}_2\text{S}$  required by cable bacteria to sustain their activity. Pore water  
574  $\sum\text{H}_2\text{S}$  was always low ( $<5 \mu\text{M}$ ). Using  $\mu\text{XRF}$  mapping of epoxy embedded sediment, we show that  
575 the activity of cable bacteria led to the development of a thin subsurface sediment layer (0.3 mm) that  
576 was highly enriched in Fe and P. The position of this layer in the sediment was directly proportional  
577 to the  $\text{O}_2$  penetration depth during the experiment. We show that a similar layer highly enriched in Fe  
578 and P was also formed in sediments of field locations populated by cable bacteria (i.e. marine Lake  
579 Grevelingen and the brackish Gulf of Finland). We suggest that such layers, which are not necessarily  
580 visible by eye, may be used as a marker of cable bacteria activity in sediments with low macrofaunal  
581 activity.

## 582 Acknowledgements

583 We are grateful to the captain and crew of R/V *Pelagia* for their support during the expedition  
584 (64PE411). We thank S. Hidalgo-Martinez for the FISH analysis and for the SEM image of the cable  
585 bacteria filaments. We thank F. Sulu-Gambari for sharing  $\mu\text{XRF}$  data for sediments from Lake  
586 Grevelingen. We also thank N. Geerlings, Z. Wang, K. Wunsch, T. Hakkert, W.K. Lenstra, N.A.G.M.  
587 van Helmond, P. Kraal, M. Egger, A. Tramper, T. Zalm and J.J. Mulder for analytical support. This  
588 research was funded by the Netherlands Organisation for Scientific Research (NWO), Vici Grant  
589 865.13.005 to CPS. Further support was provided by Research Foundation Flanders FWO Grant  
590 G038819N, NWO Vici Grant 016.VICI.170.072 to FJRM and by the Danish National Research  
591 Foundation [Agreement nos. DNRF104 and DNRF136].

## 592 References

- 593 Aller, R. 2014. Sedimentary diagenesis, depositional environments, and benthic fluxes.  
594 Aller, R. C., J. Y. Aller, Q. Zhu, C. Heilbrun, I. Klingensmith, and A. Kaushik. 2019. Worm tubes as  
595 conduits for the electrogenic microbial grid in marine sediments. *Science advances* **5**:  
596 eaaw3651.  
597 APHA. 2005. Standard methods for the examination of water and wastewater. American Public  
598 Health Association (APHA): Washington, DC, USA.



- 599 Atkinson, M. 1997. Elemental composition of commercial seasalts. *Journal of Aquaculture and*  
600 *Aquatic Sciences* **8**: 39-43.
- 601 Bellier, N., F. Chazarenc, and Y. Comeau. 2006. Phosphorus removal from wastewater by mineral  
602 apatite. *Water research* **40**: 2965-2971.
- 603 Berg, P., N. Risgaard-Petersen, and S. Rysgaard. 1998. Interpretation of measured concentration  
604 profiles in sediment pore water. *Limnology and Oceanography* **43**: 1500-1510.
- 605 Berner, R. A. 1980. *Early diagenesis: a theoretical approach*. Princeton University Press.
- 606 Bjerg, J. T., H. T. Boschker, S. Larsen, D. Berry, M. Schmid, D. Millo, P. Tataru, F. J. Meysman, M.  
607 Wagner, and L. P. Nielsen. 2018. Long-distance electron transport in individual, living cable  
608 bacteria. *Proceedings of the National Academy of Sciences* **115**: 5786-5791.
- 609 Boudreau, B. P. 1997. *Diagenetic models and their implementation*. Springer Berlin.
- 610 Boyd, P., and M. Ellwood. 2010. The biogeochemical cycle of iron in the ocean. *Nature Geoscience*  
611 **3**: 675.
- 612 Breitburg, D., L. A. Levin, A. Oschlies, M. Grégoire, F. P. Chavez, D. J. Conley, V. Garçon, D.  
613 Gilbert, D. Gutiérrez, and K. Isensee. 2018. Declining oxygen in the global ocean and coastal  
614 waters. *Science* **359**: eaam7240.
- 615 Burdige, D. J. 1993. The biogeochemistry of manganese and iron reduction in marine sediments.  
616 *Earth-Science Reviews* **35**: 249-284.
- 617 Burdige, D. J. 2006. *Geochemistry of marine sediments*. Princeton University Press.
- 618 Burdorf, L. D., S. Y. Malkin, J. T. Bjerg, P. van Rijswijk, F. Criens, A. Tramper, and F. J. Meysman.  
619 2018. The effect of oxygen availability on long-distance electron transport in marine  
620 sediments. *Limnology and Oceanography* **63**: 1799-1816.
- 621 Burdorf, L. D., A. Tramper, D. Seitaj, L. Meire, S. Hidalgo-Martinez, E.-M. Zetsche, H. T. Boschker,  
622 and F. J. Meysman. 2017. Long-distance electron transport occurs globally in marine  
623 sediments. *Biogeosciences* **14**: 683-701.
- 624 Buresh, R. J., and J. Moraghan. 1976. Chemical Reduction of Nitrate by Ferrous Iron 1. *Journal of*  
625 *Environmental Quality* **5**: 320-325.
- 626 Burton, E. D., R. T. Bush, and L. A. Sullivan. 2006. Fractionation and extractability of sulfur, iron  
627 and trace elements in sulfidic sediments. *Chemosphere* **64**: 1421-1428.
- 628 Burton, E. D., L. A. Sullivan, R. T. Bush, S. G. Johnston, and A. F. Keene. 2008. A simple and  
629 inexpensive chromium-reducible sulfur method for acid-sulfate soils. *Applied Geochemistry*  
630 **23**: 2759-2766.
- 631 Claff, S. R., L. A. Sullivan, E. D. Burton, and R. T. Bush. 2010. A sequential extraction procedure for  
632 acid sulfate soils: partitioning of iron. *Geoderma* **155**: 224-230.
- 633 Cornelissen, R., A. Bøggild, R. Thiruvallur Eachambadi, R. I. Koning, A. Kremer, S. Hidalgo-  
634 Martinez, E.-M. Zetsche, L. R. Damgaard, R. Bonn , and J. Drijkoningen. 2018. The cell  
635 envelope structure of cable bacteria. *Frontiers in microbiology* **9**: 3044.
- 636 Coull, B. C., and G. T. Chandler. 2001. Meiobenthos\*, p. 726-731. *In* J. H. Steele [ed.]. Academic  
637 Press.
- 638 Damgaard, L. R., N. Risgaard-Petersen, and L. P. Nielsen. 2014. Electric potential microelectrode for  
639 studies of electrobiogeophysics. *Journal of Geophysical Research: Biogeosciences* **119**: 1906-  
640 1917.
- 641 Davis, C. C., H.-W. Chen, and M. Edwards. 2002. Modeling silica sorption to iron hydroxide.  
642 *Environmental science & technology* **36**: 582-587.
- 643 Diaz, R. J., and R. Rosenberg. 2008. Spreading dead zones and consequences for marine ecosystems.  
644 *science* **321**: 926-929.
- 645 Egger, M., T. Jilbert, T. Behrends, C. Rivard, and C. P. Slomp. 2015. Vivianite is a major sink for  
646 phosphorus in methanogenic coastal surface sediments. *Geochimica et Cosmochimica Acta*  
647 **169**: 217-235.
- 648 Fofonoff, N. P., and R. Millard Jr. 1983. Algorithms for the computation of fundamental properties of  
649 seawater.
- 650 Fossing, H., and B. B. Jørgensen. 1989. Measurement of bacterial sulfate reduction in sediments:  
651 evaluation of a single-step chromium reduction method. *Biogeochemistry* **8**: 205-222.





- 652 Geerlings, N., E.-M. Zetsche, S. Hidalgo-Martinez, J. J. Middelburg, and F. J. Meysman. 2019.  
653 Mineral formation induced by cable bacteria performing long-distance electron transport in  
654 marine sediments. *Biogeosciences* **16**: 811-829.
- 655 Glud, R. N. 2008. Oxygen dynamics of marine sediments. *Marine Biology Research* **4**: 243-289.
- 656 Hermans, M., M. Astudillo Pascual, T. Behrends, W. K. Lenstra, D. J. Conley, and C. P. Slomp.  
657 Submitted. Coupled dynamics of iron, manganese and phosphorus in brackish coastal  
658 sediments populated by cable bacteria.
- 659 Hermans, M., W. Lenstra, S. Hidalgo-Martinez, N. A. van Helmond, R. Witbaard, F. Meysman, S.  
660 Gonzalez, and C. P. Slomp. 2019a. Abundance and Biogeochemical Impact of Cable Bacteria  
661 in Baltic Sea Sediments. *Environmental science & technology* **53**: 7494-7503.
- 662 Hermans, M., W. K. Lenstra, N. A. van Helmond, T. Behrends, M. Egger, M. J. Séguret, E.  
663 Gustafsson, B. G. Gustafsson, and C. P. Slomp. 2019b. Impact of natural re-oxygenation on  
664 the sediment dynamics of manganese, iron and phosphorus in a euxinic Baltic Sea basin.  
665 *Geochimica et Cosmochimica Acta* **246**: 174-196.
- 666 Hovanec, T. A., and J. L. Coshland. 2004. A chemical analysis of select trace elements in synthetic  
667 sea salts and natural seawater. *Sea Scope, Aquarium Systems* **21**.
- 668 Jeroschewski, P., C. Steuckart, and M. Kühl. 1996. An amperometric microsensor for the  
669 determination of H<sub>2</sub>S in aquatic environments. *Analytical Chemistry* **68**: 4351-4357.
- 670 Jilbert, T., G. de Lange, and G. J. Reichart. 2008. Fluid displacive resin embedding of laminated  
671 sediments: preserving trace metals for high-resolution paleoclimate investigations. *Limnology  
672 and Oceanography: Methods* **6**: 16-22.
- 673 Jilbert, T., and C. P. Slomp. 2013. Iron and manganese shuttles control the formation of authigenic  
674 phosphorus minerals in the euxinic basins of the Baltic Sea. *Geochimica et Cosmochimica  
675 Acta* **107**: 155-169.
- 676 Kallmeyer, J., T. G. Ferdelman, A. Weber, H. Fossing, and B. B. Jørgensen. 2004. A cold chromium  
677 distillation procedure for radiolabeled sulfide applied to sulfate reduction measurements.  
678 *Limnology and Oceanography: Methods* **2**: 171-180.
- 679 Kemp, W., J. Testa, D. Conley, D. Gilbert, and J. Hagy. 2009. Temporal responses of coastal hypoxia  
680 to nutrient loading and physical controls. *Biogeosciences* **6**: 2985-3008.
- 681 Kjeldsen, K. U., L. Schreiber, C. A. Thorup, T. Boesen, J. T. Bjerg, T. Yang, M. S. Dueholm, S.  
682 Larsen, N. Risgaard-Petersen, and M. Nierychlo. 2019. On the evolution and physiology of  
683 cable bacteria. *Proceedings of the National Academy of Sciences* **116**: 19116-19125.
- 684 Koroleff, F. 1969. Determination of ammonia as indophenol blue. *International Council for the  
685 Exploration of the Sea (ICES)* **9**.
- 686 Kraal, P., E. D. Burton, and R. T. Bush. 2013. Iron monosulfide accumulation and pyrite formation in  
687 eutrophic estuarine sediments. *Geochimica et Cosmochimica Acta* **122**: 75-88.
- 688 Kraal, P., N. Dijkstra, T. Behrends, and C. P. Slomp. 2017. Phosphorus burial in sediments of the  
689 sulfidic deep Black Sea: Key roles for adsorption by calcium carbonate and apatite  
690 authigenesis. *Geochimica et Cosmochimica Acta* **204**: 140-158.
- 691 Kraal, P., and C. P. Slomp. 2014. Rapid and extensive alteration of phosphorus speciation during oxic  
692 storage of wet sediment samples. *PloS one* **9**: e96859.
- 693 Kraal, P., C. P. Slomp, A. Forster, M. M. Kuypers, and A. Sluijs. 2009. Pyrite oxidation during  
694 sample storage determines phosphorus fractionation in carbonate-poor anoxic sediments.  
695 *Geochimica et Cosmochimica Acta* **73**: 3277-3290.
- 696 Kristensen, E., K. D. Kristiansen, and M. H. Jensen. 2003. Temporal behavior of manganese and iron  
697 in a sandy coastal sediment exposed to water column anoxia. *Estuaries* **26**: 690-699.
- 698 Kristensen, E., G. Penha-Lopes, M. Delefosse, T. Valdemarsen, C. O. Quintana, and G. T. Banta.  
699 2012. What is bioturbation? The need for a precise definition for fauna in aquatic sciences.  
700 *Marine Ecology Progress Series* **446**: 285-302.
- 701 Kristiansen, K., E. Kristensen, and E. Jensen. 2002. The influence of water column hypoxia on the  
702 behaviour of manganese and iron in sandy coastal marine sediment. *Estuarine, Coastal and  
703 Shelf Science* **55**: 645-654.
- 704 Kuz'minskii, Y. V., A. Andriiko, and L. Nyrkova. 1994. Chemical and phase composition of  
705 manganese oxides obtained by Mn (II) oxidation in nitrate solutions. *Journal of power sources*  
706 **52**: 49-53.



- 707 Larsen, S., L. P. Nielsen, and A. Schramm. 2015. Cable bacteria associated with long-distance  
708 electron transport in New England salt marsh sediment. *Environmental microbiology reports*  
709 **7**: 175-179.
- 710 Learman, D., B. Voelker, A. Vazquez-Rodriguez, and C. Hansel. 2011. Formation of manganese  
711 oxides by bacterially generated superoxide. *Nature Geoscience* **4**: 95.
- 712 Lenstra, W., M. Hermans, M. Séguret, R. Witbaard, T. Behrends, N. Dijkstra, N. Van Helmond, P.  
713 Kraal, P. Laan, and M. Rijkenberg. 2019. The shelf-to-basin iron shuttle in the Black Sea  
714 revisited. *Chemical Geology* **511**: 314-341.
- 715 Lenstra, W., M. Séguret, T. Behrends, R. Groeneveld, M. Hermans, R. Witbaard, and C. Slomp. 2020.  
716 Controls on the shuttling of manganese over the northwestern Black Sea shelf and its fate in  
717 the euxinic deep basin. *Geochimica et Cosmochimica Acta* **273**: 177-204.
- 718 Luther, G. W. 2010. The role of one-and two-electron transfer reactions in forming  
719 thermodynamically unstable intermediates as barriers in multi-electron redox reactions.  
720 *Aquatic Geochemistry* **16**: 395-420.
- 721 Madison, A. S., B. M. Tebo, A. Mucci, B. Sundby, and G. W. Luther. 2013. Abundant porewater Mn  
722 (III) is a major component of the sedimentary redox system. *science* **341**: 875-878.
- 723 Malkin, S. Y., A. M. Rao, D. Seitaj, D. Vasquez-Cardenas, E.-M. Zetsche, S. Hidalgo-Martinez, H. T.  
724 Boschker, and F. J. Meysman. 2014. Natural occurrence of microbial sulphur oxidation by  
725 long-range electron transport in the seafloor. *The ISME journal* **8**: 1843-1854.
- 726 Malkin, S. Y., D. Seitaj, L. D. Burdorf, S. Nieuwhof, S. Hidalgo-Martinez, A. Tramper, N. Geeraert,  
727 H. De Stigter, and F. J. Meysman. 2017. Electrogenic sulfur oxidation by cable bacteria in  
728 bivalve reef sediments. *Frontiers in Marine Science* **4**: 28.
- 729 Marzocchi, U., D. Trojan, S. Larsen, R. L. Meyer, N. P. Revsbech, A. Schramm, L. P. Nielsen, and N.  
730 Risgaard-Petersen. 2014. Electric coupling between distant nitrate reduction and sulfide  
731 oxidation in marine sediment. *The ISME journal* **8**: 1682-1690.
- 732 Meysman, F. J. 2018. Cable bacteria take a new breath using long-distance electricity. *Trends in*  
733 *microbiology* **26**: 411-422.
- 734 Meysman, F. J., R. Cornelissen, S. Trashin, R. Bonné, S. H. Martinez, J. van der Veen, C. J. Blom, C.  
735 Karman, J.-L. Hou, and R. T. Eachambadi. 2019. A highly conductive fibre network enables  
736 centimetre-scale electron transport in multicellular cable bacteria. *Nature communications* **10**:  
737 1-8.
- 738 Meysman, F. J., N. Risgaard-Petersen, S. Y. Malkin, and L. P. Nielsen. 2015. The geochemical  
739 fingerprint of microbial long-distance electron transport in the seafloor. *Geochimica et*  
740 *Cosmochimica Acta* **152**: 122-142.
- 741 Millero, F. J., T. Plese, and M. Fernandez. 1988. The dissociation of hydrogen sulfide in seawater 1.  
742 *Limnology and Oceanography* **33**: 269-274.
- 743 Morgan, B., E. D. Burton, and A. W. Rate. 2012. Iron monosulfide enrichment and the presence of  
744 organosulfur in eutrophic estuarine sediments. *Chemical Geology* **296**: 119-130.
- 745 Müller, H., J. Bosch, C. Griebler, L. R. Damgaard, L. P. Nielsen, T. Lueders, and R. U. Meckenstock.  
746 2016. Long-distance electron transfer by cable bacteria in aquifer sediments. *The ISME*  
747 *journal* **10**: 2010-2019.
- 748 Murphy, J., and J. Riley. 1958. A single-solution method for the determination of soluble phosphate in  
749 sea water. *Journal of the Marine Biological Association of the United Kingdom* **37**: 9-14.
- 750 Naudet, V., and A. Revil. 2005. A sandbox experiment to investigate bacteria-mediated redox  
751 processes on self-potential signals. *Geophysical Research Letters* **32**.
- 752 Nielsen, L. P., and N. Risgaard-Petersen. 2015. Rethinking sediment biogeochemistry after the  
753 discovery of electric currents. *Annual review of marine science* **7**: 425-442.
- 754 Nielsen, L. P., N. Risgaard-Petersen, H. Fossing, P. B. Christensen, and M. Sayama. 2010. Electric  
755 currents couple spatially separated biogeochemical processes in marine sediment. *Nature* **463**:  
756 1071-1074.
- 757 Norkko, J., D. C. Reed, K. Timmermann, A. Norkko, B. G. Gustafsson, E. Bonsdorff, C. P. Slomp, J.  
758 Carstensen, and D. J. Conley. 2012. A welcome can of worms? Hypoxia mitigation by an  
759 invasive species. *Global Change Biology* **18**: 422-434.
- 760 Nriagu, J. O. 1972. Stability of vivianite and ion-pair formation in the system  $Fe_3(PO_4)_2 \cdot$   
761  $H_3PO_4 \cdot H_2O$ . *Geochimica et Cosmochimica Acta* **36**: 459-470.



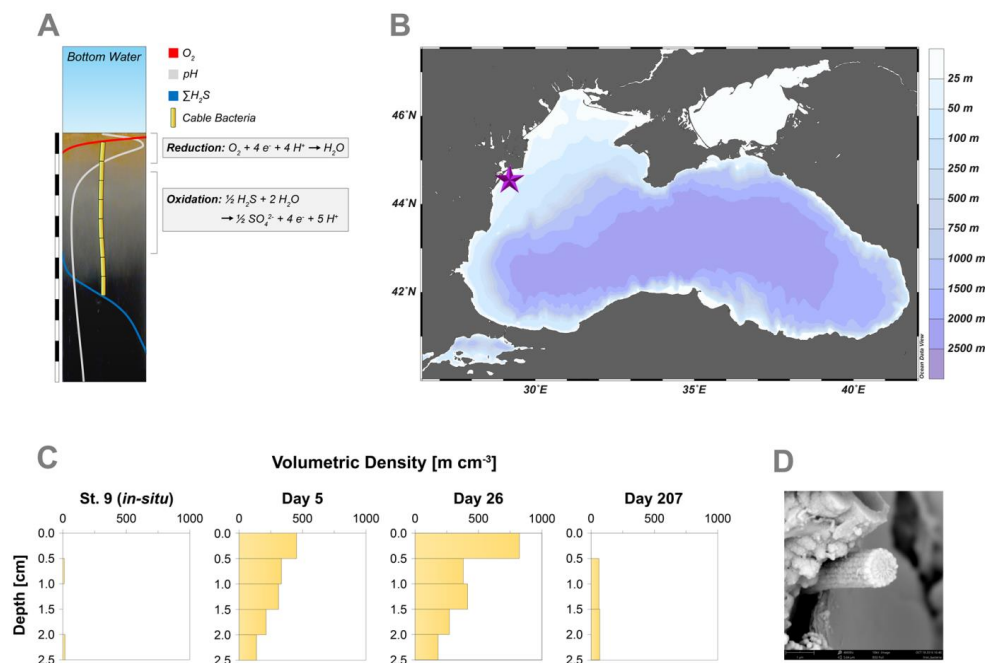
- 762 Pernthaler, J., F.-O. Glöckner, W. Schönhuber, and R. Amann. 2001. Fluorescence in situ  
763 hybridization (FISH) with rRNA-targeted oligonucleotide probes. *Methods in microbiology*  
764 **30**: 207-226.
- 765 Pfeffer, C., S. Larsen, J. Song, M. Dong, F. Besenbacher, R. L. Meyer, K. U. Kjeldsen, L. Schreiber,  
766 Y. A. Gorby, and M. Y. El-Naggar. 2012. Filamentous bacteria transport electrons over  
767 centimetre distances. *Nature* **491**: 218-221.
- 768 Poulton, S. W., and D. E. Canfield. 2005. Development of a sequential extraction procedure for iron:  
769 implications for iron partitioning in continentally derived particulates. *Chemical Geology*  
770 **214**: 209-221.
- 771 Rabalais, N. N., W.-J. Cai, J. Carstensen, D. J. Conley, B. Fry, X. Hu, Z. Quinones-Rivera, R.  
772 Rosenberg, C. P. Slomp, and R. E. Turner. 2014. Eutrophication-driven deoxygenation in the  
773 coastal ocean. *Oceanography* **27**: 172-183.
- 774 Rabalais, N. N., R. E. Turner, and W. J. Wiseman Jr. 2002. Gulf of Mexico hypoxia, aka “The dead  
775 zone”. *Annual Review of ecology and Systematics* **33**: 235-263.
- 776 Rabouille, C., L. Denis, K. Dedieu, G. Stora, B. Lansard, and C. Grenz. 2003. Oxygen demand in  
777 coastal marine sediments: comparing in situ microelectrodes and laboratory core incubations.  
778 *Journal of Experimental Marine Biology and Ecology* **285**: 49-69.
- 779 Raiswell, R., and D. E. Canfield. 2012. The iron biogeochemical cycle past and present. *Geochemical*  
780 *perspectives* **1**: 1-2.
- 781 Rao, A. M., S. Y. Malkin, S. Hidalgo-Martinez, and F. J. Meysman. 2016. The impact of electrogenic  
782 sulfide oxidation on elemental cycling and solute fluxes in coastal sediment. *Geochimica et*  
783 *Cosmochimica Acta* **172**: 265-286.
- 784 Rasmussen, H., and B. B. Jørgensen. 1992. Microelectrode studies of seasonal oxygen uptake in a  
785 coastal sediment: role of molecular diffusion. *Marine ecology progress series*. Oldendorf **81**:  
786 289-303.
- 787 Reed, D. C., C. P. Slomp, and B. G. Gustafsson. 2011. Sedimentary phosphorus dynamics and the  
788 evolution of bottom-water hypoxia: A coupled benthic–pelagic model of a coastal system.  
789 *Limnology and Oceanography* **56**: 1075-1092.
- 790 Revil, A., M. Karaoulis, T. Johnson, and A. Kemna. 2012. Some low-frequency electrical methods for  
791 subsurface characterization and monitoring in hydrogeology. *Hydrogeology Journal* **20**: 617-  
792 658.
- 793 Revil, A., C. Mendonça, E. Atekwana, B. Kulesa, S. Hubbard, and K. Bohlen. 2010. Understanding  
794 biogeobatteries: Where geophysics meets microbiology. *Journal of Geophysical Research*:  
795 *Biogeosciences* **115**.
- 796 Riedel, B., M. Zuschin, and M. Stachowitsch. 2012. Tolerance of benthic macrofauna to hypoxia and  
797 anoxia in shallow coastal seas: a realistic scenario. *Marine Ecology Progress Series* **458**: 39-  
798 52.
- 799 Risgaard-Petersen, N., M. Kristiansen, R. B. Frederiksen, A. L. Dittmer, J. T. Bjerg, D. Trojan, L.  
800 Schreiber, L. R. Damgaard, A. Schramm, and L. P. Nielsen. 2015. Cable bacteria in  
801 freshwater sediments. *Applied and environmental microbiology* **81**: 6003-6011.
- 802 Risgaard-Petersen, N., A. Revil, P. Meister, and L. P. Nielsen. 2012. Sulfur, iron-, and calcium  
803 cycling associated with natural electric currents running through marine sediment.  
804 *Geochimica et Cosmochimica Acta* **92**: 1-13.
- 805 Risgaard-Petersen, N., L. R. Damgaard, A. Revil, and L. P. Nielsen. 2014. Mapping electron sources  
806 and sinks in a marine biogeobattery. *Journal of Geophysical Research: Biogeosciences* **119**:  
807 1475-1486.
- 808 Ruttenberg, K. C. 1992. Development of a sequential extraction method for different forms of  
809 phosphorus in marine sediments. *Limnology and oceanography* **37**: 1460-1482.
- 810 Ruttenberg, K. C., and R. A. Berner. 1993. Authigenic apatite formation and burial in sediments from  
811 non-upwelling, continental margin environments. *Geochimica et cosmochimica acta* **57**: 991-  
812 1007.
- 813 Sandfeld, T., U. Marzocchi, C. Petro, A. Schramm, and N. Risgaard-Petersen. 2020. Electrogenic  
814 sulfide oxidation mediated by cable bacteria stimulates sulfate reduction in freshwater  
815 sediments. *The ISME Journal* **14**: 1233-1246.



- 816 Schauer, R., N. Risgaard-Petersen, K. U. Kjeldsen, J. J. T. Bjerg, B. B. Jørgensen, A. Schramm, and  
817 L. P. Nielsen. 2014. Succession of cable bacteria and electric currents in marine sediment.  
818 *The ISME journal* **8**: 1314.
- 819 Schmidtko, S., L. Stramma, and M. Visbeck. 2017. Decline in global oceanic oxygen content during  
820 the past five decades. *Nature* **542**: 335.
- 821 Seitaj, D., R. Schauer, F. Sulu-Gambari, S. Hidalgo-Martinez, S. Y. Malkin, L. D. Burdorf, C. P.  
822 Slomp, and F. J. Meysman. 2015. Cable bacteria generate a firewall against euxinia in  
823 seasonally hypoxic basins. *Proceedings of the National Academy of Sciences* **112**: 13278-  
824 13283.
- 825 Sigg, L., and W. Stumm. 1981. The interaction of anions and weak acids with the hydrous goethite ( $\alpha$ -  
826 FeOOH) surface. *Colloids and surfaces* **2**: 101-117.
- 827 Slomp, C. P., E. H. Epping, W. Helder, and W. V. Raaphorst. 1996. A key role for iron-bound  
828 phosphorus in authigenic apatite formation in North Atlantic continental platform sediments.  
829 *Journal of Marine Research* **54**: 1179-1205.
- 830 Soetaert, K., T. Petzoldt, and F. Meysman. 2010. Marelac: Tools for aquatic sciences. R package  
831 version.
- 832 Straub, K. L., M. Benz, B. Schink, and F. Widdel. 1996. Anaerobic, nitrate-dependent microbial  
833 oxidation of ferrous iron. *Appl. Environ. Microbiol.* **62**: 1458-1460.
- 834 Sulu-Gambari, F., M. Hagens, T. Behrends, D. Seitaj, F. J. Meysman, J. Middelburg, and C. P. Slomp.  
835 2018. Phosphorus cycling and burial in sediments of a seasonally hypoxic Marine Basin.  
836 *Estuaries and Coasts* **41**: 921-939.
- 837 Sulu-Gambari, F., D. Seitaj, T. Behrends, D. Banerjee, F. J. Meysman, and C. P. Slomp. 2016a.  
838 Impact of cable bacteria on sedimentary iron and manganese dynamics in a seasonally-  
839 hypoxic marine basin. *Geochimica et Cosmochimica Acta* **192**: 49-69.
- 840 Sulu-Gambari, F., D. Seitaj, F. J. Meysman, R. Schauer, L. Polerecky, and C. P. Slomp. 2016b. Cable  
841 bacteria control iron-phosphorus dynamics in sediments of a coastal hypoxic basin.  
842 *Environmental science & technology* **50**: 1227-1233.
- 843 Trojan, D., L. Schreiber, J. T. Bjerg, A. Bøggild, T. Yang, K. U. Kjeldsen, and A. Schramm. 2016. A  
844 taxonomic framework for cable bacteria and proposal of the candidate genera *Electrothrix* and  
845 *Electronema*. *Systematic and applied microbiology* **39**: 297-306.
- 846 Van Cappellen, P., and R. A. Berner. 1988. A mathematical model for the early diagenesis of  
847 phosphorus and fluorine in marine sediments; apatite precipitation. *American Journal of*  
848 *Science* **288**: 289-333.
- 849 van de Velde, S., L. Lesven, L. D. Burdorf, S. Hidalgo-Martinez, J. S. Geelhoed, P. Van Rijswijk, Y.  
850 Gao, and F. J. Meysman. 2016. The impact of electrogenic sulfur oxidation on the  
851 biogeochemistry of coastal sediments: A field study. *Geochimica et Cosmochimica Acta* **194**:  
852 211-232.
- 853 Vasquez-Cardenas, D., J. Van De Vossenberg, L. Polerecky, S. Y. Malkin, R. Schauer, S. Hidalgo-  
854 Martinez, V. Confurius, J. J. Middelburg, F. J. Meysman, and H. T. Boschker. 2015.  
855 Microbial carbon metabolism associated with electrogenic sulphur oxidation in coastal  
856 sediments. *The ISME journal* **9**: 1966.
- 857 Wang, Y., and P. Van Cappellen. 1996. A multicomponent reactive transport model of early  
858 diagenesis: Application to redox cycling in coastal marine sediments. *Geochimica et*  
859 *Cosmochimica Acta* **60**: 2993-3014.
- 860 Wijsman, J. W., J. J. Middelburg, P. M. Herman, M. E. Böttcher, and C. H. Heip. 2001. Sulfur and  
861 iron speciation in surface sediments along the northwestern margin of the Black Sea. *Marine*  
862 *Chemistry* **74**: 261-278.



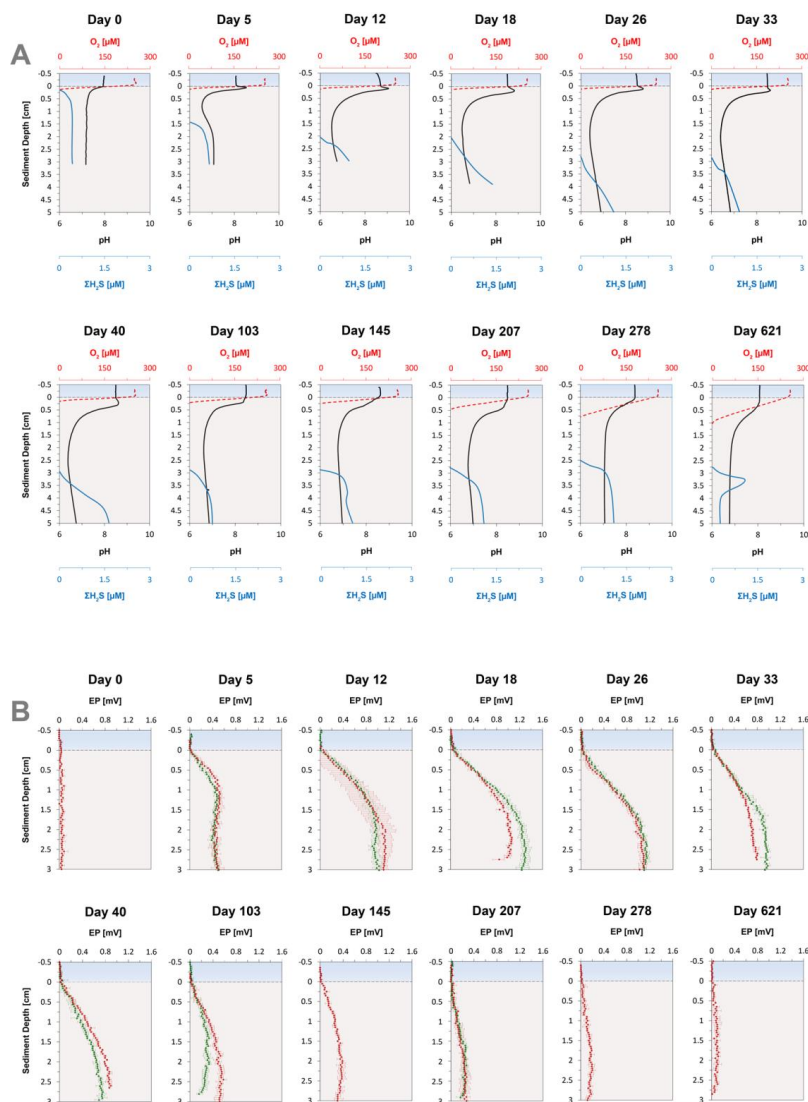
863 **FIGURES AND TABLES**



864

865 **Fig. 1.** (A) Geochemical pore water fingerprint typical for cable bacteria activity. This fingerprint is defined by a distinct pH  
 866 pH profile (light grey line) and a sub-oxic zone that is devoid of  $O_2$  (red line) and  $H_2S$  (blue line). The cable bacteria filaments  
 867 are depicted in yellow. On the background, the sediment core photograph, taken 278 days after the start of the experiment,  
 868 shows a distinct colour zonation where (1) the oxic zone displays an orange colour (2) the suboxic zone has a grey colour  
 869 and (3) the sulphidic zone has a black colour. The scale bar denotes a distance of 6 cm, with 0.5 cm intervals. (B)  
 870 Bathymetric map of the Black Sea. The purple star indicates the location of our study site (44°34.93'N, 29°11.38' E), which  
 871 was sampled with R/V *Pelagia* in September 2015. Further details are provided in Lenstra et al. (2019). (C) Volumetric  
 872 density of cable bacteria [ $m\ cm^{-3}$ ] in the top 2.5 cm of the sediment, for *in-situ* as well as for three time points during the  
 873 incubation experiment (D) SEM image of a cable bacteria filament that was extracted from the surface sediment after 40  
 874 days.

875



876

877 **Fig. 2.** (A) Time-series of the pore water pH (black), O<sub>2</sub> (red) and ΣH<sub>2</sub>S (blue) signatures of the incubated sediment. (B)

878 Development of the EP depth profile in the incubated sediment over time. The dashed-line at 0 mm depth represents the

879 sediment-water interface. The blue boxes indicate the overlying water, whereas the underlying light grey boxes represent the

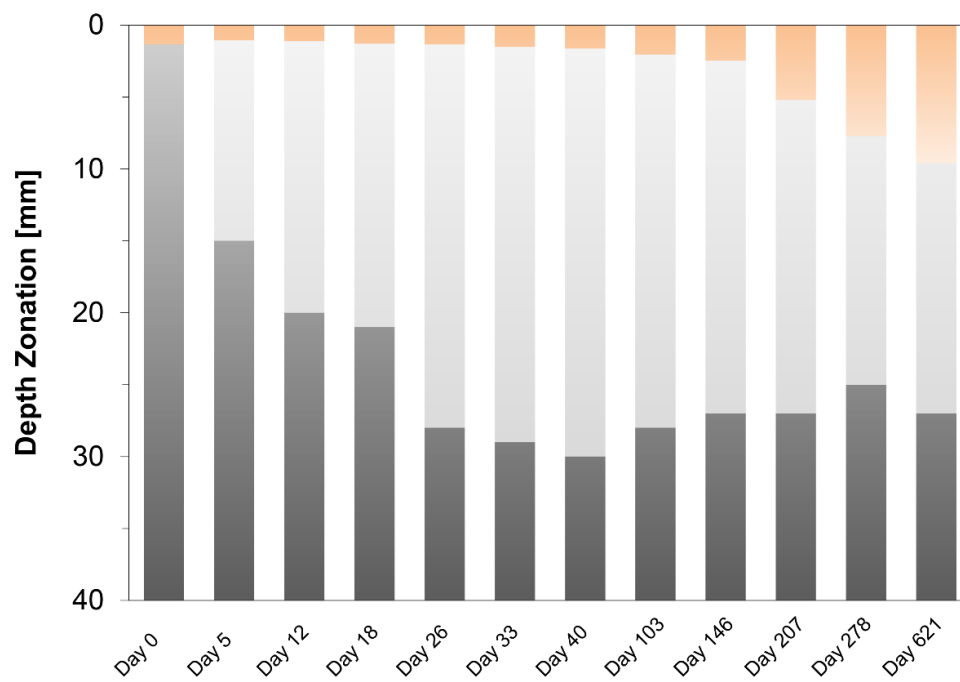
880 sediment. The EP depth profiles represent an average of 3 replicate measurements. The error bars indicate the minimum and

881 maximum EP values that were observed. The green depth profiles represent duplicate measurement performed on a different

882 core.

883





884

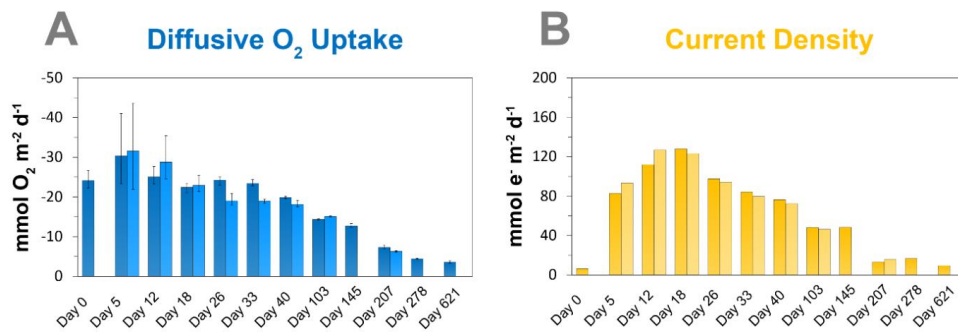
885 **Fig. 3.** Time-series of the development of the oxic zone (orange), suboxic zone (light grey) and the anoxic/sulphidic zone

886 (dark grey) in the sediment. These zones were calculated from 3 replicate measurements on two different cores.

887



888

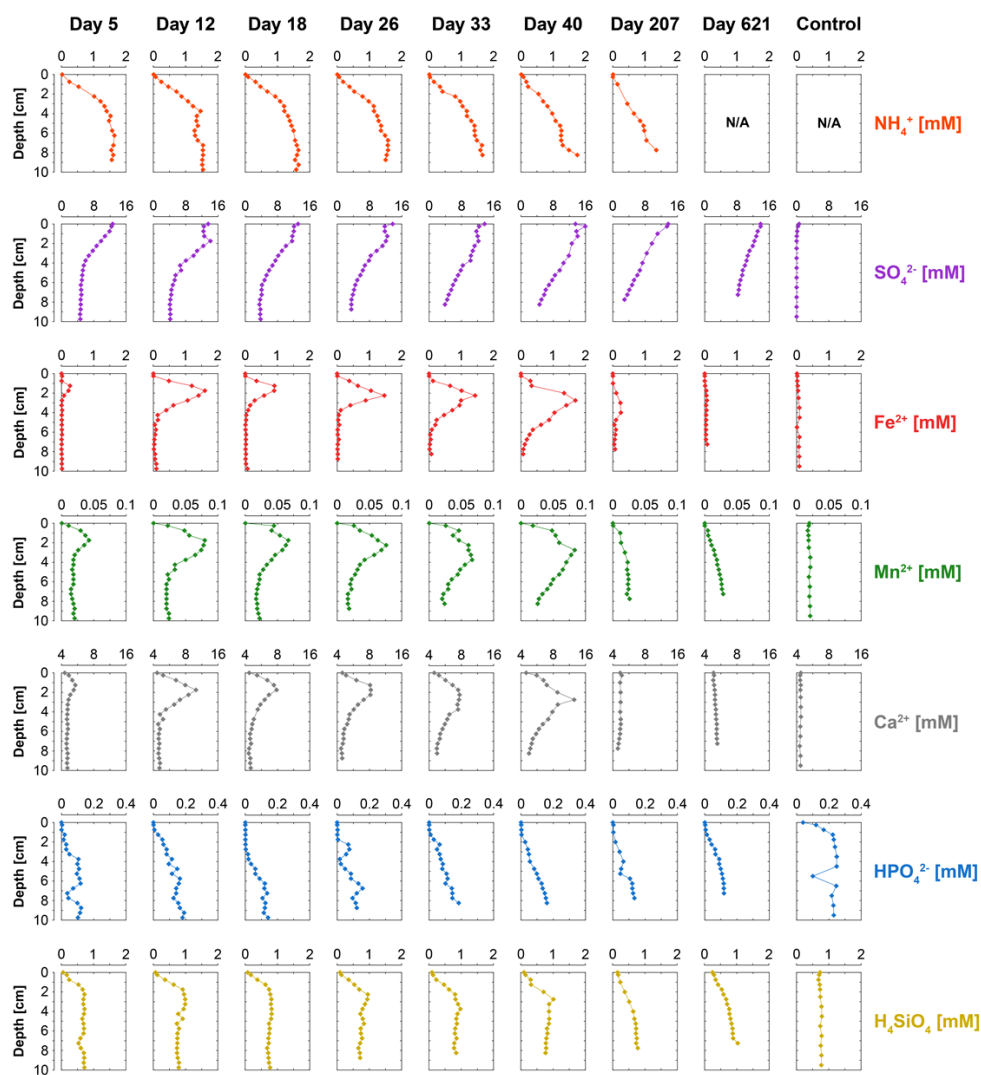


889

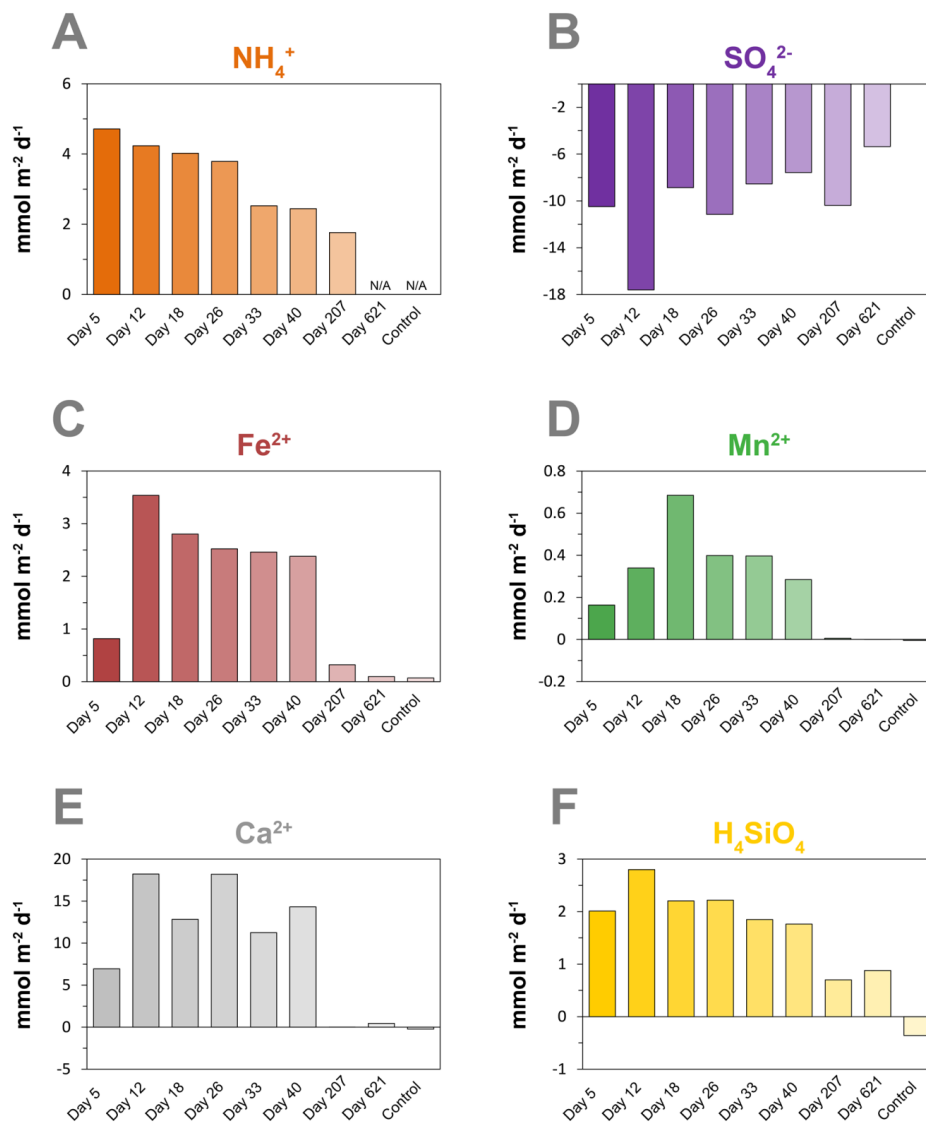
890 **Fig. 4.** Time-series of the (A) diffusive O<sub>2</sub> uptake in mmol O<sub>2</sub> m<sup>-2</sup> d<sup>-1</sup> and (B) current density as a consequence of long-  
891 distance electron transport (e<sup>-</sup>) in mmol e<sup>-</sup> m<sup>-2</sup> d<sup>-1</sup> in the sediment incubation.

892





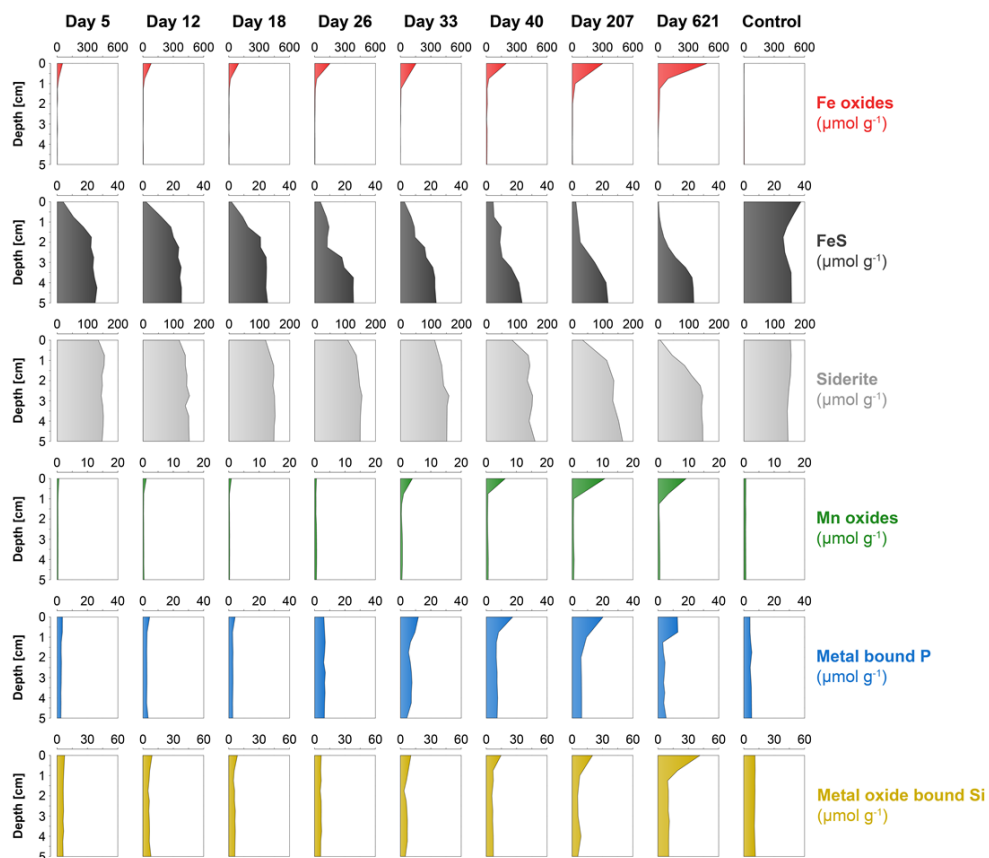
894 **Fig. 5.** Time-series of pore water depth profiles of  $\text{NH}_4^+$  (orange),  $\text{SO}_4^{2-}$  (purple),  $\text{Fe}^{2+}$  (red),  $\text{Mn}^{2+}$  (green),  $\text{Ca}^{2+}$  (grey),  
895  $\text{HPO}_4^{2-}$  (blue) and  $\text{H}_4\text{SiO}_4$  (yellow). The control core was sampled at day 621.



896

897 **Fig. 6.** Time-series of diffusive fluxes calculated from the linear gradient of the pore water profiles of (A)  $\text{NH}_4^+$ , (B)  $\text{SO}_4^{2-}$ ,  
898 (C)  $\text{Fe}^{2+}$ , (D)  $\text{Mn}^{2+}$ , (E)  $\text{Ca}^{2+}$  and (F)  $\text{H}_4\text{SiO}_4$  in  $\text{mmol m}^{-2} \text{d}^{-1}$  towards the oxic zone of the sediment, based on the linear pore  
899 water gradients (Section 1.6; Fig. S3-S4). Here, a positive value indicates an upward flux, whereas a negative value  
900 represents a downward flux. N/A = not available. The control core was sampled at day 621.

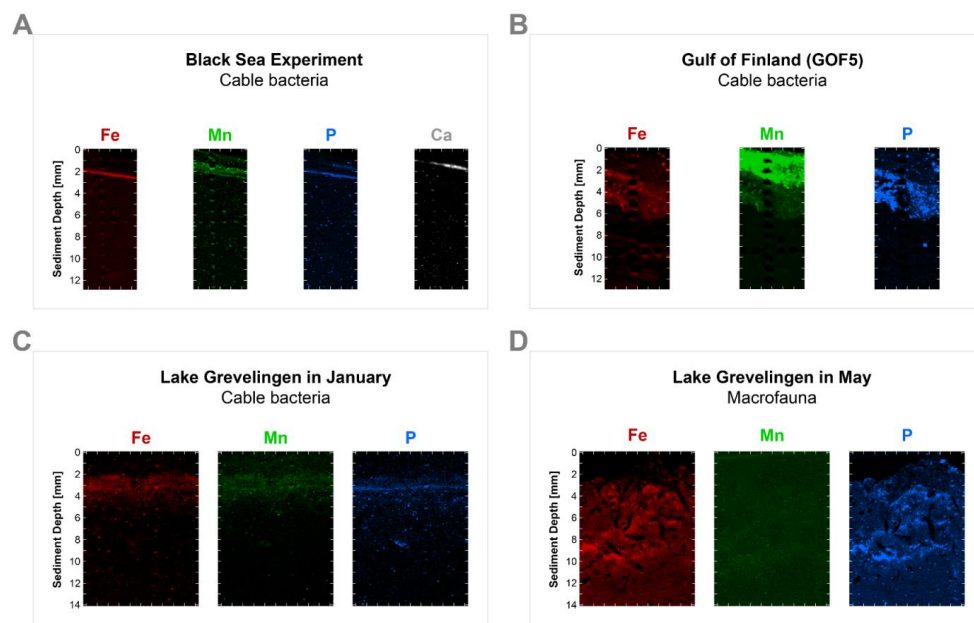
901



902

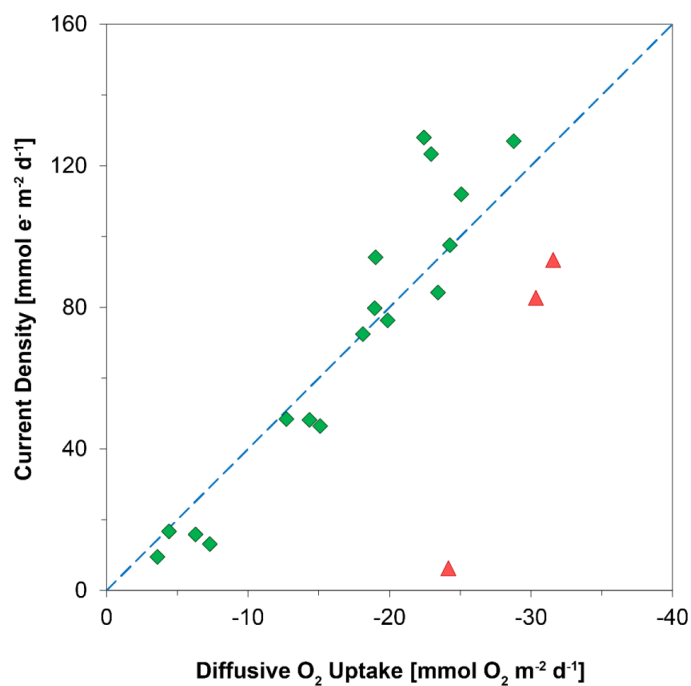
903 **Fig. 7.** Time-series of solid-phase depth profiles of Fe oxides (red), FeS (black), siderite (grey), Mn oxides (green), metal

904 bound P (blue) and metal oxide bound Si (yellow).



905

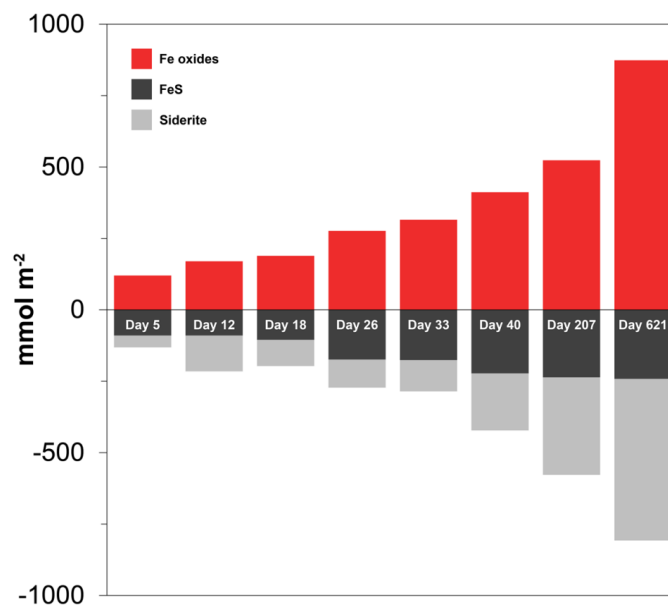
906 **Fig. 8.** High-resolution elemental maps of Fe (red), Mn (green), P (blue) and Ca (white) of surface sediments. These maps  
907 are shown in true vertical orientation and the colours accentuate the relative count intensities adjusted for brightness and  
908 contrast to highlight the features in the sediment. The tick marks represent 1 mm intervals.  $\mu$ XRF maps of the surface  
909 sediment (A) from the incubation experiment, (B) from the Gulf of Finland at site GOF5 in June (Hermans et al. Submitted),  
910 (C) from Lake Grevelingen in January (when cable bacteria become active) and (D) from Lake Grevelingen in May  
911 (showing the effects of bioturbation as described in Seitaj et al. (2015)).  
912



913

914 **Fig. 9.** The relationship between the diffusive uptake of O<sub>2</sub> (mmol O<sub>2</sub> m<sup>-2</sup> d<sup>-1</sup>) and the current density of long-distance  
915 electron transport (mmol e<sup>-</sup> m<sup>-2</sup> d<sup>-1</sup>). Red triangles are data for days 0 and 5. Green diamonds are data for all other time  
916 points. The blue line represents the expected correlation between the cathodic O<sub>2</sub> consumption rate and the current density  
917 assuming a 1:4 ratio (Nielsen et al. 2010). Here, a positive value indicates an upward flux, whereas a negative value  
918 represents a downward flux.

919



920

921 **Fig. 10.** Time-series of the depth integrated (0-5 cm) increase in Fe oxides (red) and the depletion of FeS (black) and siderite  
922 (grey) in  $\text{mmol m}^{-2}$ . Negative values represent a decrease, whereas positive values indicate an increase in the mineral pools.

923



924 **Table 1.** Key site characteristics: latitude, longitude, water depth, bottom water O<sub>2</sub> concentration, *in-situ* O<sub>2</sub> uptake, *in-situ*  
 925 O<sub>2</sub> penetration depth in the sediment, porosity and salinity. These data were retrieved from Lenstra et al. (2019). Our study  
 926 site is station 9 in Lenstra et al. (2019).

Black Sea (Station 9)		Unit
Latitude	44°34.9'	N
Longitude	29°11.4'	E
Water depth	27	m
Bottom water O <sub>2</sub>	92	μM
O <sub>2</sub> uptake	25.8 ± 1.77	mmol m <sup>-2</sup> d <sup>-1</sup>
O <sub>2</sub> penetration depth	2.25	mm
Porosity	0.86	-
Salinity	17.881	-

927  
 928 **Table 2.** Mass balance of O<sub>2</sub> consumption. The diffusive uptake of O<sub>2</sub> as calculated from the O<sub>2</sub> depth profiles (column 1)  
 929 was compared to the potential O<sub>2</sub> demand from the oxidation of NH<sub>4</sub><sup>+</sup>, Fe<sup>2+</sup> and Mn<sup>2+</sup> (column 2-4). The O<sub>2</sub> consumption of  
 930 the oxidation of NH<sub>4</sub><sup>+</sup>, Fe<sup>2+</sup> and Mn<sup>2+</sup> was determined based on the stoichiometry of NH<sub>4</sub><sup>+</sup>, Fe<sup>2+</sup> and Mn<sup>2+</sup> oxidation with O<sub>2</sub>  
 931 as described in Reed et al. (2011). The oxidation of dissolved Fe<sup>2+</sup> and Mn<sup>2+</sup> only played a minor role in the total O<sub>2</sub>  
 932 consumption during the experiment, contributing only 0.9 to 3.8% and 0.1 to 0.4%, respectively.

	O <sub>2</sub> [mmol m <sup>-2</sup> d <sup>-1</sup> ]	Potential O <sub>2</sub> Demand			e <sup>-</sup> [mmol m <sup>-2</sup> d <sup>-1</sup> ]
		NH <sub>4</sub> <sup>+</sup> [mmol m <sup>-2</sup> d <sup>-1</sup> ]	Fe <sup>2+</sup> [mmol m <sup>-2</sup> d <sup>-1</sup> ]	Mn <sup>2+</sup> [mmol m <sup>-2</sup> d <sup>-1</sup> ]	
Day 5	-23.35	9.42	0.21	0.05	82.68
Day 12	-23.24	8.46	0.89	0.09	111.94
Day 18	-21.10	8.04	0.70	0.08	127.97
Day 26	-23.00	7.58	0.63	0.07	97.55
Day 33	-22.80	5.06	0.62	0.05	84.16
Day 40	-19.60	4.88	0.60	0.06	76.31
Day 207	-6.90	3.52	0.08	0.01	13.10
Day 621	-3.25	N/A	0.03	0.01	9.47

933



934 **Table 3.** Mass balance of Fe. Time-series of the depth integrated (0-5 cm) increase in Fe oxides and the depth integrated (0-5  
 935 cm) depletion of FeS and FeCO<sub>3</sub> (siderite) in mmol m<sup>-2</sup>. All values are reported in mmol Fe m<sup>-2</sup>. Negative values represent a  
 936 decrease, whereas positive values indicate an increase in the mineral pools.

	$\Delta\text{Fe oxides}$ [mmol m <sup>-2</sup> ]	$\Delta\text{FeS}$ [mmol m <sup>-2</sup> ]	$\Delta\text{FeCO}_3$ [mmol m <sup>-2</sup> ]
Day 5	120	-90	-42
Day 12	170	-90	-126
Day 18	189	-105	-92
Day 26	276	-174	-99
Day 33	315	-176	-109
Day 40	412	-223	-200
Day 207	523	-236	-341
Day 621	874	-242	-566

937  
 938 **Table 4.** Sources of  $\Sigma\text{H}_2\text{S}$  calculated from the reduction of SO<sub>4</sub><sup>2-</sup> and the dissolution of FeS. The numbers are presented  
 939 either as mmol m<sup>-2</sup> d<sup>-1</sup> or as the relative percentage of the  $\Sigma\text{H}_2\text{S}$  production. The amount of S from the dissolution of FeS  
 940 was estimated from the upward diffusive flux of Fe<sup>2+</sup> (Fig. 6C) and the relative fraction of FeS (FeS/FeS+siderite) based on  
 941 the mass balance calculations (Table 3).

	S from SO <sub>4</sub> <sup>2-</sup> reduction [mmol m <sup>-2</sup> d <sup>-1</sup> ]	S from FeS dissolution [mmol m <sup>-2</sup> d <sup>-1</sup> ]	S from SO <sub>4</sub> <sup>2-</sup> reduction [%]	S from FeS dissolution [%]
Day 5	10.49	0.56	95%	5%
Day 12	17.60	1.48	92%	8%
Day 18	8.87	1.50	86%	14%
Day 26	11.15	1.61	87%	13%
Day 33	8.54	1.52	85%	15%
Day 40	7.57	1.25	86%	14%
Day 207	10.38	0.13	99%	1%
Day 621	5.36	0.03	99%	1%

942